CANCER

MerTK$^+$ macrophages promote melanoma progression and immunotherapy resistance through AhR-ALKAL1 activation

Naming Wu[1,2]†, Jun Li[3]†, Lu Li[1,2], Liu Yang[1,2], Liyun Dong[1,2], Chen Shen[1,2], Shanshan Sha[1,2], Yangxue Fu[1,2], Enzhu Dong[1,2], Fang Zheng[4], Zheng Tan[4], Juan Tao[1,2]*

Despite our increasing understanding of macrophage heterogeneity, drivers of macrophage phenotypic and functional polarization in the microenvironment are not fully elucidated. Here, our single-cell RNA sequencing data identify a subpopulation of macrophages expressing high levels of the phagocytic receptor MER proto-oncogene tyrosine kinase (MerTK$^+$ macrophages), which is closely associated with melanoma progression and immunotherapy resistance. Adoptive transfer of the MerTK$^+$ macrophages into recipient mice notably accelerated tumor growth regardless of macrophage depletion. Mechanistic studies further revealed that ALK And LTK Ligand 1 (ALKAL1), a target gene of aryl hydrocarbon receptor (AhR), facilitated MerTK phosphorylation, resulting in heightened phagocytic activity of MerTK$^+$ macrophages and their subsequent polarization toward an immunosuppressive phenotype. Specifically targeted delivery of AhR antagonist to tumor-associated macrophages with mannosylated micelles could suppress MerTK expression and improved the therapeutic efficacy of anti–programmed cell death ligand 1 therapy. Our findings shed light on the regulatory mechanism of MerTK$^+$ macrophages and provide strategies for improving the efficacy of melanoma immunotherapy.

INTRODUCTION

Melanoma is the most common primary malignancy of the skin with a low survival rate worldwide (*1*). Over the past decade, cancer immunotherapy has achieved significant breakthroughs (*2*, *3*). In particular, immune checkpoint blockade (ICB) therapies have yielded remarkable clinical responses and revolutionized the treatment of many cancers (*4*). The Food and Drug Administration has to date approved cytotoxic T lymphocyte antigen–4 (CTLA-4) and programmed cell death protein–1/ligand 1 (PD-1/PD-L1) blockade therapies for treating various malignancies (*5*). However, only a small fraction of patients respond to these therapies, the effectiveness of which may be greatly limited by the immunosuppressive tumor microenvironment (TME) (*6*, *7*). To overcome immunotherapeutic tolerance, tumor-induced immune-suppressive mechanisms have been a focus of considerable research in recent years, and multiple suppressor cell populations in the TME have now been identified, among which the tumor-associated macrophages (TAMs) have stood out as novel emerging targets for immunotherapy in malignant cancers (*8*).

TAMs are a major and heterogeneous distinct immune cell subpopulation in the immunosuppressive TME and play an essential role in enhancing tumor malignancy and suppressing antitumor immunity (*9*, *10*). Depending on the surrounding immune environment, macrophages can be polarized toward an immunostimulatory phenotype by proinflammatory stimuli [e.g., interferon-γ (IFN-γ) and lipopolysaccharide (LPS)] or toward an immunosuppressive phenotype by anti-inflammatory stimuli [e.g., interleukin-4 (IL-4) and IL-13] (*11*). In established solid tumors, TAMs predominately exhibit an immunosuppressive phenotype, evidenced by their production of anti-inflammatory cytokines and arginase-1 (Arg1), as well as their expression of mannose receptor (CD206) and scavenger receptors (*12*, *13*). In addition, TAMs can inhibit T cell activities through immune checkpoint engagement by expressing the ligands of the inhibitory receptors PD-1 and CTLA-4 (*12*). It has been demonstrated also that TAMs show plasticity and can switch functions in response to environmental cues in the TME, resulting in functional heterogeneity with diverse phenotypes (*14*). These characteristics of TAMs make them potential targets for reversing the immunosuppressive TME to augment antitumor immunity. Nevertheless, the functional phenotypes of macrophage subpopulations and their underlying mechanisms are not yet completely understood.

In this study, using single-cell analysis, we identified a subpopulation of MER proto-oncogene tyrosine kinase (MerTK$^+$) macrophages in melanoma that displays potent immunosuppressive activity. We found that MerTK phosphorylation and activation are dependent on the aryl hydrocarbon receptor (AhR)–mediated transcription of ALKAL1, thereby resulting in enhanced phagocytosis of MerTK$^+$ macrophages and polarization toward an immunosuppressive phenotype with elevated expression of Arg1, CD206, and PD-L1 in vitro. We found in vivo that the adoptive transfer of MerTK$^+$ macrophages, but not MerTK$^-$ macrophages, into recipient mice of either macrophage-depleted wild-type or Lyz2$^{cre/+}$Ahr$^{fl/fl}$ mice accelerated tumor growth by suppressing T cell function. Furthermore, we also demonstrated that specifically targeted delivery of AhR antagonist to TAMs with mannosylated micelles could suppress MerTK expression and improved the efficacy of anti–PD-L1 (aPD-L1) therapy in tumor-bearing mouse models. Our present findings suggest that AhR-ALKAL1 signaling is a critical regulator of MerTK$^+$ macrophages and a promising target for melanoma immunotherapy.

[1]Department of Dermatology, Union Hospital, Tongji Medical College, Huazhong University of Science and Technology (HUST), Wuhan 430022, China. [2]Hubei Engineering Research Center for Skin Repair and Theranostics, Wuhan 430022, China. [3]Department of Dermatology, The Central Hospital of Wuhan, Tongji Medical College, Huazhong University of Science and Technology (HUST), Wuhan 430022, China. [4]Department of Immunology, School of Basic Medicine, Tongji Medical College, Huazhong University of Science and Technology (HUST), Wuhan, China.
*Corresponding author. Email: tjhappy@126.com
†These authors contributed equally to this work.

RESULTS

The concentration of MerTK$^+$ macrophages in the TME are closely related to melanoma stage and immunotherapy response

Immunotherapeutic strategies including ICB therapies have demonstrated durable responses in a small proportion of patients with melanoma, but most of these cases still show only a limited clinical effect, and some are totally unresponsive (*15*, *16*). TAMs are a major component of the immunosuppressive TME and are often correlated with a poor prognosis and resistance to treatment, including to immunotherapies (*9*, *17*). Considering the phenotypic heterogeneity of myeloid cells, we here performed single-cell RNA sequencing (scRNA-seq) to map myeloid subsets in the tumors of three patients with melanoma. Transcriptome profiling was performed on individual CD45$^+$ immune cells isolated from these tumor tissues (Table 1 and fig. S1A). We initially assessed the composition of the tumor-infiltrating immune cells (TIIs) and identified distinct lineages based on their signature genes (*18*), which included CD4$^+$ T cells, CD8$^+$ T cells, regulatory T cells, B cells, dendritic cells, monocytes, and macrophages (Fig. 1A and fig. S1, B and C). We used gene signatures to further stratify the monocytes and macrophages into three subsets (Fig. 1, B and C, and fig. S1, D and E). Compared with monocytes, macrophages can most notably be characterized by the abundant expression of *MerTK* and *CD163* (fig. S1F). The first subset was identified as monocytes on the basis of the high expression of *Lyz*, *Timp1*, *Gos2*, and *IL-1β* (fig. S1, G and H). Notably, MerTK was found to be highly expressed in the Mac c2 subset but less so in the Mac c1 subset and in the monocytes (Fig. 1D). Functional enrichment analysis suggested that the Mac c1 subset (hereafter referred to as MerTK$^-$ macrophages) was enriched for predicted functions mainly in antigen processing and presentation (fig. S1I). In contrast, the Mac c2 subset appeared to mainly function in macrophage phagocytosis (hereafter referred to as MerTK$^+$ macrophages; Fig. 1E). The expression of MerTK showed a positive correlation with *CD163* in MerTK$^+$ macrophages (Fig. 1F). Furthermore, *MerTK* expression was found to be positively correlated with *CD163* in melanomas from The Cancer Genome Atlas (TCGA) skin cutaneous melanoma (SKCM) datasets and from a patient cohort receiving anti–PD-1 treatment (Fig. 1, G and H). Immunofluorescent costaining of MerTK and CD163 indicated that the frequency of MerTK$^+$ macrophages in tumor tissues gradually increased from tumor clinicopathologic stage I to stage IV in patients with melanoma (Fig. 1, I and J). In addition, compared with

Table 1. Clinicopathological characteristics of the melanoma cohort treated with anti–PD-1 therapy, related to Fig. 1.

Patient characteristics	Melanoma (*n* = 42)	+ Anti–PD-1 therapy (*n* = 12)	All patients (*n* = 54)
Age (years), median	64	68	65.5
Sex, *n* (%)			
Male	27 (64.3%)	3 (25.0%)	30 (55.6%)
Female	15 (35.7%)	9 (75.0%)	24 (44.4%)
Breslow depth (mm), *n* (%)			
≤1 mm	5 (11.9%)	1 (8.3%)	6 (11.1%)
1.01 to 2 mm	8 (19.0%)	1 (8.3%)	9 (16.7%)
2.01 to 4 mm	12 (28.6%)	5 (41.7%)	17 (31.5%)
>4 mm	10 (23.8%)	4 (33.3%)	14 (25.9%)
Unknown	7 (16.7%)	1 (8.3%)	8 (14.8%)
Clark class, *n* (%)			
1	0 (0%)	0 (0%)	0 (0%)
2	6 (14.3%)	0 (0%)	6 (11.1%)
3	8 (19.0%)	3 (25.0%)	11 (20.4%)
4	15 (35.7%)	6 (50.0%)	21 (38.9%)
5	10 (23.8%)	1 (8.3%)	11 (20.4%)
Unknown	3 (7.1%)	2 (16.7%)	5 (9.3%)
Stage of diagnosis, *n* (%)			
I	9 (21.4%)	0 (0%)	9 (16.7%)
II	20 (47.6%)	2 (16.7%)	22 (40.7%)
III	8 (19.0%)	7 (58.3%)	15 (27.8%)
IV	2 (4.8%)	2 (16.7%)	4 (7.4%)
Unknown	3 (7.1%)	1 (8.3%)	4 (7.4%)
Metastasis, *n* (%)			
Yes	8 (19.0%)	9 (75.0%)	17 (31.5%)
No	33 (78.6%)	2 (16.7%)	35 (64.8%)
Unknown	1 (2.4%)	1 (8.3%)	2 (3.7%)
Anti–PD-1			

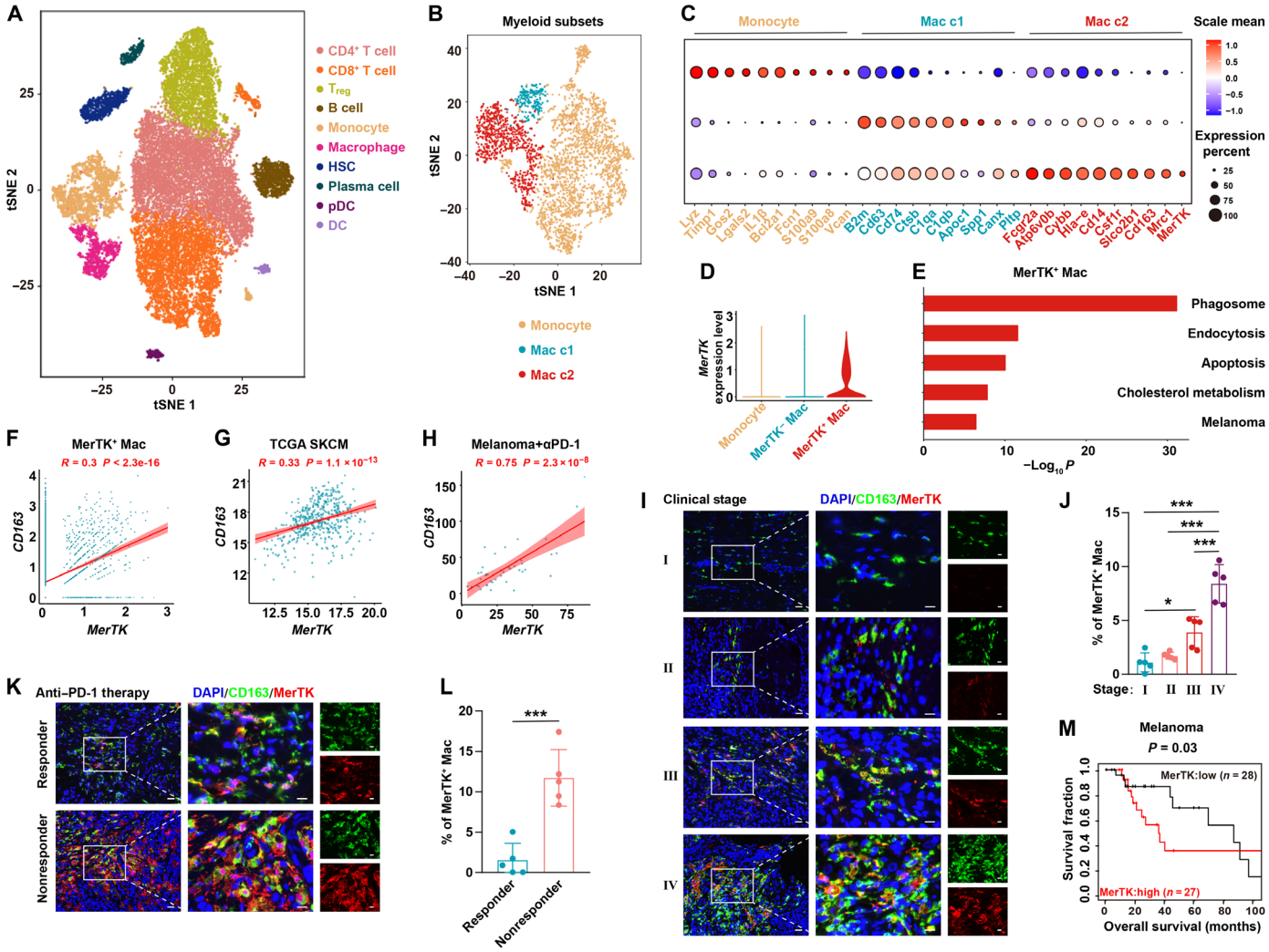

Fig. 1. The concentration of MerTK$^+$ macrophages in the TME are closely related to melanoma stage and immunotherapy response. (**A**) T-distributed stochastic neighbor embedding (t-SNE) plots showing cellular landscapes based on detailed cell typing. (**B**) A t-SNE plot displaying three clusters of myeloid cells from scRNA-seq, including the monocyte and two macrophage subsets (Mac c1 and Mac c2). (**C**) Bubble heatmap showing the expression of representative genes for each subset shown in (B). (**D**) Violin plots showing the expression of MerTK across the identified immune cell populations according to (A). (**E**) Function enrichment analysis showing the functions of MerTK$^+$ macrophages (MerTK$^+$ Mac). (**F**) Expression correlation between MerTK and CD163 in MerTK$^+$ Mac from scRNA-seq. (**G** and **H**) Expression correlation between MerTK and marker gene of macrophages CD163 in TCGA SKCM (G) and a melanoma patient cohort with anti–PD-1 therapy [our analysis of data published in (*57*); (H)]. (**I**) Representative combined staining of CD163 (green), MerTK (red), and 4′,6-diamidino-2-phenylindole (DAPI) (blue) in tumor tissues of various clinicopathologic stages of patients with melanoma. Scale bars, 25 μm (left panel) and 10 μm (all other panels). (**J**) Quantification of MerTK$^+$ Mac shown in (I). (**K**) Representative combined staining of CD163 (green), MerTK (red), and DAPI (blue) in tumor tissues of responders and nonresponders of patients with melanoma treated with anti–PD-1 monoclonal antibodies. Scale bars, 25 μm (left panel) and 10 μm (all other panels). (**L**) Quantification of MerTK$^+$ Mac shown in (K). (**M**) Kaplan-Meier analysis of OS curves for melanoma patient datasets from TCGA. Data are means ± SEM, and *P* values were using a Spearman's rank correlation coefficient [(F) to (H)], one-way analysis of variance (ANOVA) (J), a two-sided Student's *t* test (L) or by two-sided Wald test in a Cox–proportional hazard (PH) regression (M). $^*P < 0.05$, $^{**}P < 0.01$, and $^{***}P < 0.001$.

responders among patients with melanoma treated with anti–PD-1 monoclonal antibodies, nonresponders expressed a higher frequency of MerTK$^+$ macrophages in their tumor tissues (Fig. 1, K and L).

We next examined the serum levels of MerTK in healthy controls and patients with melanoma. Compared with healthy controls, MerTK expression was increased in primary melanoma and elevated further in metastatic melanoma (fig. S2A). An analysis of diagnostic value using a receiver operating characteristic curve indicated that the serum concentration of MerTK in most patients with melanoma was higher than 7.0487 pg/ml compared with the healthy controls. Notably, if the cutoff of the serum MerTK level was set at 7.9515 pg/ml, it was an even more notable factor in distinguishing primary from metastatic melanoma (fig. S2B). The results from analysis of SKCM samples in TCGA also indicated a higher expression of MerTK in metastatic than in primary melanoma (fig. S2, C and D). Furthermore, the MerTK expression level was negatively correlated with patient overall survival (OS) in multiple cancer patient cohorts spanning melanoma, breast cancer, liver hepatocellular carcinoma, stomach adenocarcinoma, and adrenocortical carcinoma (Fig. 1M and fig. S2E). We additionally observed a statistically positive correlation between MerTK expression and the

immune infiltration of macrophages, especially those of the M2 phenotype (Fig. 1F and fig. S2G). These data are consistent with MerTK$^+$ macrophages being central mediators of an immunosuppressed TME as the disease grade worsens.

Analysis of specific ligand-receptor interactions revealed a unique pattern of interactions between MerTK$^+$ macrophages and effector CD8$^+$ T cells based on molecules associated with the Cxcl12/Cxcr4 pathway (fig. S3, A and B). Having established the importance of CD8$^+$ T cells, we next determined the phenotypic characteristics of these cells to gain insights into their potential role in tumor control. As described before, the total numbers of CD8$^+$ T cells expanded during anti–PD-1 treatment, most notably tumor-resident memory CD8$^+$ T cells characterized by their constitutive surface expression of CD69 and CD103 (fig. S3, C to F) (*19*, *20*), which is in contrast to the expression trend of MerTK$^+$ macrophages. Together, our current data demonstrated that the concentration of MerTK$^+$ macrophages is closely related to tumor malignancy and immunotherapy resistance, indicating their crucial role in the tumor immunosuppressive microenvironment.

MerTK$^+$ macrophages promote tumor growth

As MerTK$^+$ macrophages play an important role in the staging of cancer and response to immunotherapy in melanoma, we investigated whether they could contribute to tumor progression. To test this possibility, mice were initially depleted of macrophages by the administration of Clophosome liposomes as described (*21*, *22*). Local injections of Clophosome liposomes were intended to eliminate early recruitment of macrophages and subsequently adoptively transferred MerTK$^+$ macrophages into tumor-bearing mice (Fig. 2A). Flow cytometry analysis also confirmed a reduction in the number of TAMs 6 days after Clophosome liposome injection (Fig. 2B). Immunofluorescence further confirmed TAM depletion after Clophosome liposome treatment (Fig. 2C). We then isolated MerTK$^+$ macrophages (identified as CD45$^+$F4/80$^+$CD11b$^+$MerTK$^+$ cells) from tumor single-cell suspensions through fluorescence-activated cell sorting (FACS; fig. S4). We found that depletion of macrophages by Clophosome liposomes successfully recused tumor growth as expected. Notably, adoptive transfer of MerTK$^+$ macrophages into recipient mice restored tumor growth in mice regardless of macrophage depletion, while MerTK$^-$ macrophages did not promote tumor growth (Fig. 2, D to F). Notably, removal of macrophages followed by MerTK$^+$ macrophage adoptive transfer resulted in a substantial increase in tumor growth, even beyond normal levels in mice (Fig. 2, D to F). Compared to MerTK$^-$ macrophages, the purified sorted MerTK$^+$ macrophages expressed greater PD-L1 (Fig. 2G). Moreover, we observed a decrease in the percentages of CD8$^+$ T cells, along with reduced percentages of IFN-γ^+ and tumor necrosis factor–α–positive (TNF-α^+) CD4$^+$ and CD8$^+$ T cells in MerTK$^+$ macrophage adoptive transfer group regardless of macrophage clearance (Fig. 2, H and I). Higher level of immune checkpoint PD-1 expression was also observed in MerTK$^+$ macrophage adoptive transfer group (Fig. 2J). These data collectively indicated that MerTK$^+$ macrophages exacerbate tumor progression by impairing T cell functions.

AhR is highly expressed in MerTK$^+$ macrophages and promotes MerTK-mediated phagocytosis

To further characterize the functional phenotype of the two observed macrophage subsets, we generated a volcano plot to compare the differentially expressed genes between MerTK$^-$ and MerTK$^+$ macrophages of the scRNA-seq. We revealed that MerTK$^-$ macrophages exhibited a high expression of the complement genes *C1qa* and *C1qb*, antigen presentation–related gene *B2m*, and the cellular signaling cascade–related genes *Cd63* and *Timp1*. The high expression of phagocytic-related genes *MerTK*, *Cd163*, *Mrc1*, and *Fcgr2a*, chemokine-related genes *Ccl3*, *Ccl3l1*, *Ccl4*, and *Ccl4l2*, and environmental sensor–related gene *AhR* was detected in MerTK$^+$ macrophages (Fig. 3A). AhR expression was also confirmed to be significantly higher in MerTK$^+$ macrophages (Fig. 3B). The colocalization of CD163, AhR, and MerTK was detected in melanoma by multiplex immunofluorescence staining. The quantification of CD163$^+$AhR$^+$MerTK$^+$ macrophages in tumor tissues are gradually increased from tumor clinicopathological stages I to IV (Fig. 3, C and D). Furthermore, higher levels of CD163$^+$AhR$^+$MerTK$^+$ macrophages were observed in nonresponders among patients with melanoma treated with anti–PD-1 monoclonal antibodies (Fig. 3, E and F).

The phagocytosis of apoptotic cells in the TME is mainly performed by macrophages, a process known as efferocytosis, and involves various receptors, the most common of which is the MerTK receptor (*23*–*25*). Given the fact that high expression of AhR was detected in MerTK$^+$ macrophages, we investigated whether AhR could regulate MerTK-mediated phagocytosis. We cultured bone marrow–derived macrophages (BMDMs) in vitro and polarized macrophages toward an immunosuppressive M2 phenotype (fig. S5A). RNA sequencing (RNA-seq) analysis was used to identify the AhR-regulated genes in AhR agonist kynurenine (Kyn)– or antagonist CH22319–treated M2 macrophages. The most significant enrichment of AhR regulated genes was associated with phagocytosis pathways (Fig. 3G). Next, the function of AhR in macrophages was explored in an in vitro model of phagocytosis using BMDMs cocultured with PKH26-labeled apoptotic thymocytes or pHrodo bioparticles. With the coincubation time extended from 30 to 180 min, we found that CH223191 substantially suppressed the engulfment of apoptotic thymocytes and pHrodo bioparticles by the BMDMs. In contrast, Kyn promoted phagocytosis efficiency (Fig. 3, H and I, and fig. S5, B to D). Thus, AhR functions to promote the phagocytosis of macrophages.

We further investigated whether AhR functions to promote the MerTK-mediated phagocytosis of macrophages. We found that MerTK expression was up-regulated in IL-4–induced M2 macrophages at both the mRNA and protein levels. Furthermore, our results showed that CH223191 reduced, while Kyn enhanced, the expression of MerTK in IL-4–induced M2 macrophages (Fig. 3J and fig. S5E). Previous research has demonstrated that MerTK phosphorylation and activation are required for MerTK-mediated phagocytosis (*26*, *27*). We thus examined the phosphorylation of MerTK and found that CH223191 decreased, while Kyn increased, the MerTK phosphorylation level in IL-4–induced M2 macrophages (Fig. 3K). Together, these data suggested that AhR plays an important role in MerTK phosphorylation and activation to promote the MerTK-mediated phagocytosis of macrophages to remove apoptotic cells.

AhR-mediated ALKAL1 transcription promotes MerTK activation and expression

To further explore the underlying molecular mechanism of AhR-regulated phosphorylation and expression of MerTK, we used chromatin immunoprecipitation (ChIP) to examine the binding site

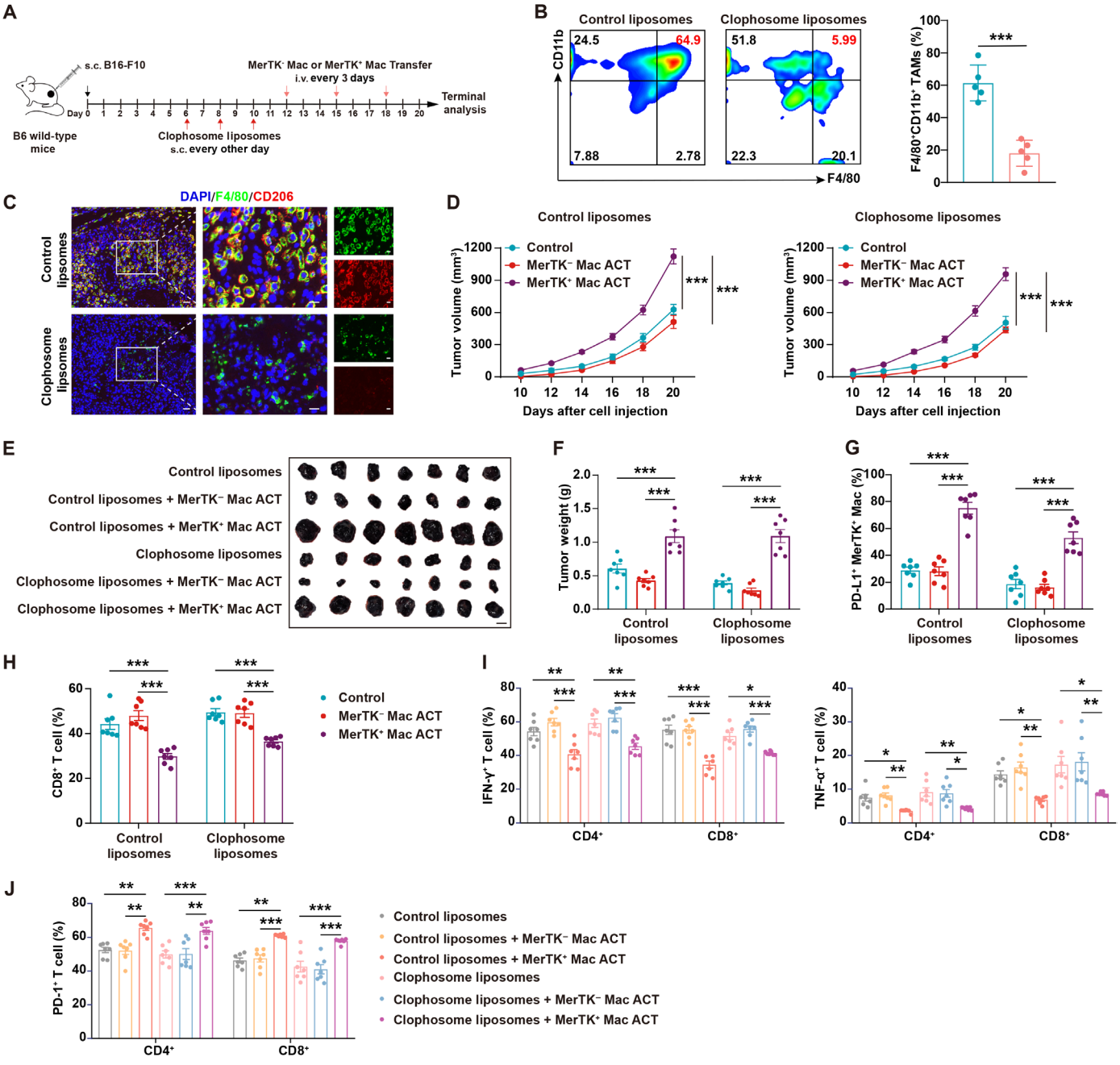

Fig. 2. MerTK$^+$ macrophages promote tumor growth. [(A) to (J)] Studying the effects of MerTK$^+$ Mac in a B16-F10 melanoma syngeneic mouse tumor model. (**A**) Adoptive transfer method. (**B** and **C**) Tumor tissues were isolated at day 12 after the subcutaneous injection of control liposomes or Clophosome liposomes at days 6, 8, and 10. (B) Flow cytometry analysis of the percentages of TAMs (F4/80$^+$CD11b$^+$ cells) in B16-F10 tumors at day 12 after implantation. (C) Representative combined staining of F4/80 (green), CD206 (red), and DAPI (blue) in tumor tissues. Scale bars, 25 μm (left panel) and 10 μm (all other panels). (**D**) Tumor growth. (**E**) Subcutaneous B16-F10 tumors were surgically removed and presented. Scale bar, 1 cm. (**F**) Tumor weight. (**G**) Flow cytometry analysis of the percentages of PD-L1$^+$ cells in MerTK$^+$ Mac. (**H**) Flow cytometry analysis of the percentages of CD8$^+$ T cells in CD3$^+$ T cells. (**I** and **J**) Flow cytometry analysis of the percentages of cells expressing IFN-γ and TNF-α (I) and PD-1 (J) in CD4$^+$ and CD8$^+$ T cells. Representative of three experiments. Data are means ± SEM, and *P* values were determined by a two-sided Student's *t* test (B), one-way ANOVA (D) or two-way ANOVA [(F) to (J)]. **P* < 0.05, ***P* < 0.01, and ****P* < 0.001. g, gram.

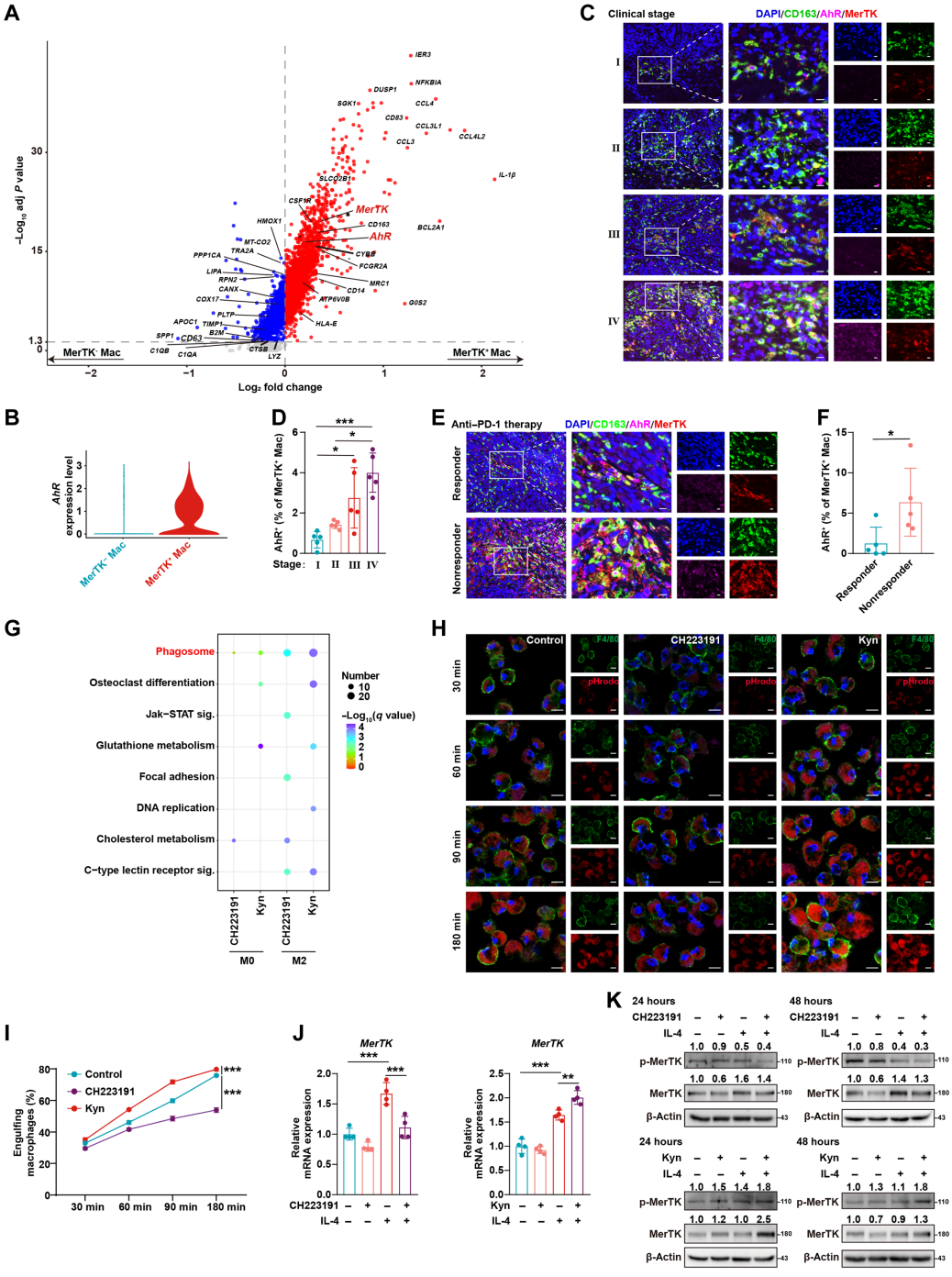

Fig. 3. AhR is highly expressed in MerTK$^+$ macrophages and promotes MerTK-mediated phagocytosis. (**A**) Volcano plot showing differentially expressed genes between MerTK$^-$ Mac and MerTK$^+$ Mac from the scRNA-seq. (**B**) Violin plot showing the expression of *AhR* in MerTK$^-$ Mac and MerTK$^+$ Mac. (**C**) Representative combined staining of CD163 (green), AhR (pink), MerTK (red), and DAPI (blue) in tumor tissues of various clinicopathologic stages of patients of melanoma. Scale bars, 25 μm (left panel) and 10 μm (all other panels). (**D**) Quantification of AhR$^+$ in MerTK$^+$ Mac shown in (C). (**E**) Representative combined staining of CD163 (green), AhR (pink), MerTK (red), and DAPI (blue) in tumor tissues of responders and nonresponders of patients with melanoma treated with anti–PD-1 monoclonal antibodies. Scale bars, 25 μm (left panel) and 10 μm (all other panels). (**F**) Quantification of AhR$^+$ in MerTK$^+$ Mac shown in (E). (**G**) RNA-seq analysis of signaling pathway enrichment analysis of up-regulated genes in BMDMs. (**H** and **I**) BMDMs were incubated with pHrodo *E. coli* BioParticle conjugates (H) or PKH26-labeled apoptotic thymocytes (Ap) (I) for 30, 60, 90, and 180 min. (H) Shown are representative confocal images of BMDMs (green) engulfing BioParticle (red). DAPI (blue) was the nuclear stain. Scale bar, 10 μm. (I) Flow cytometry analysis of the percentages of engulfing macrophages. (**J**) Reverse transcription polymerase chain reaction (RT-PCR) analysis of *MerTK* mRNA expression. (**K**) Western blot analysis of phosphorylated (denoted by p-) and total MerTK proteins. One representative donor of four is shown. Numbers depict the quantification of Western blot bands relative to β-actin. Representative of three experiments. Data are means ± SEM, and *P* values were determined by one-way ANOVA [(D), (I), and (J)] or by a two-sided Student's *t* test (F). **P* < 0.05, ***P* < 0.01, and ****P* < 0.001.

of AhR responsive elements in BMDMs. In light of the strong regulatory interaction between AhR, we characterized how it influences the chromatin occupancy of AhR binding partners in BMDMs. ChIP sequencing (ChIP-seq) analysis was performed to identify direct AhR target genes in BMDMs. We found significant enrichment of ChIP-seq peaks distributed across the genome, corresponding to 120 unique common genes (Fig. 4A). Among the direct AhR targets, we picked *ALKAL1*, an activating ligand for anaplastic lymphoma kinase (ALK; Fig. 4B) (*28*). Both MerTK and ALK belong to the same family of receptor tyrosine kinases (RTKs) (*29*, *30*). Motif analysis with Homer was used to investigate genome-wide AhR-enriched sites (Fig. 4C). In addition, ChIP–polymerase chain reaction (PCR) analysis confirmed a specific enrichment of ALKAL1 (Fig. 4D). We observed that CH223191 could decrease, while Kyn increased, the

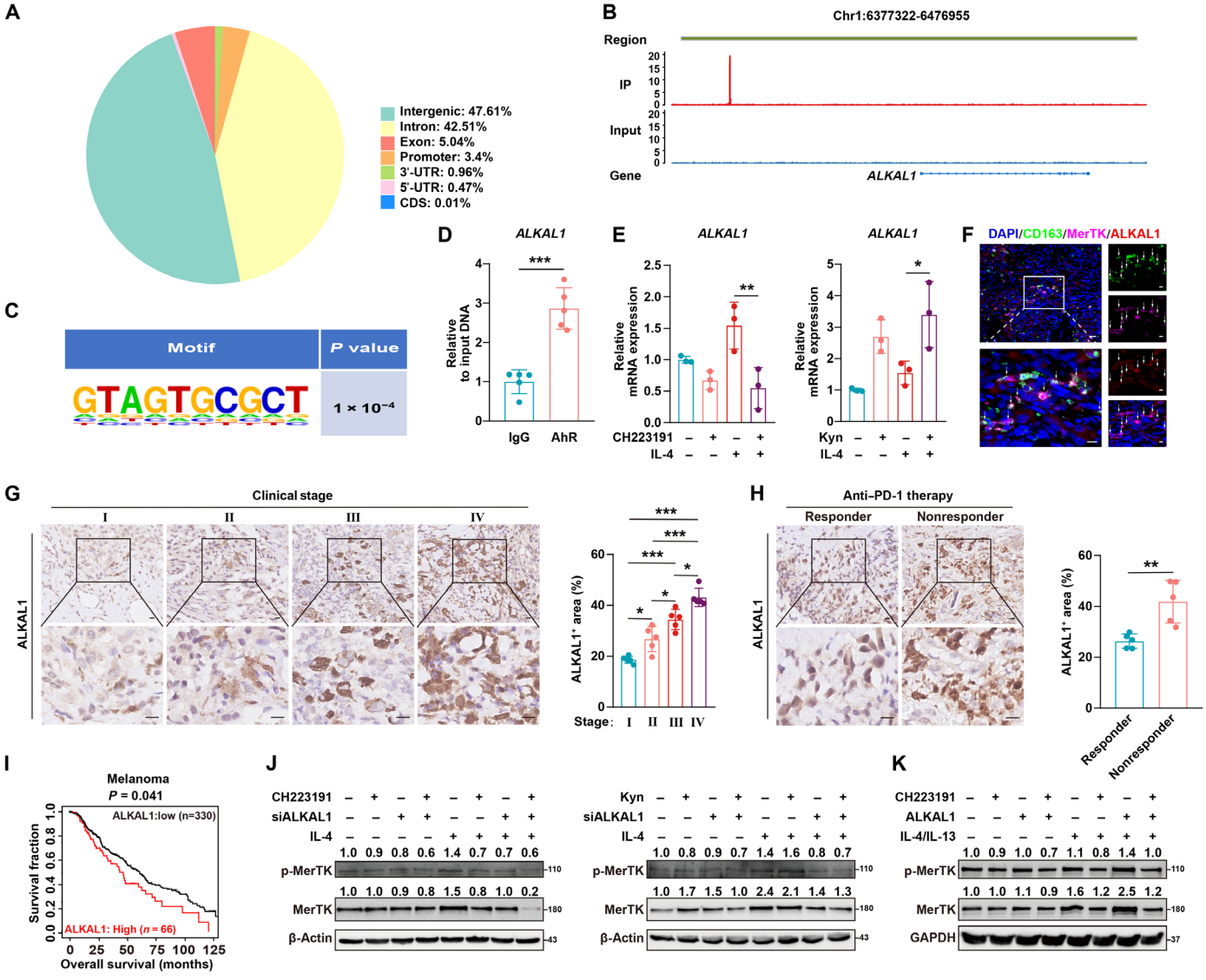

Fig. 4. AhR-mediated ALKAL1 transcription promotes MerTK activation and expression. (**A**) Peak locations across the genome. The numbers indicate the percentages for ChIP-seq distribution. (**B**) Representative ChIP-seq peak located on the AhR direct target gene revealed using a genome browser Integrative Genomics Viewer. (**C**) Homer known motif enrichment result. (**D**) ChIP-PCR analysis of the selected AhR binding sites. RT-PCR was performed with the indicated primer pair using an anti-AhR antibody immunoprecipitated DNA fragment as the template. Normal mouse IgG was used as negative control. (**E**) RT-PCR analysis of *ALKAL1* mRNA expression. (**F**) Representative combined staining of CD163 (green), MerTK (pink), ALKAL1 (red), and DAPI (blue) in tumor tissues of patients with melanoma. Scale bars, 25 μm (left panel) and 10 μm (all other panels). (**G** and **H**) Representative photomicrographs of immunohistochemical analysis for ALKAL1 expression in tumor tissues at various clinicopathologic stages (G), of responders and nonresponders of patients with melanoma treated with anti–PD-1 monoclonal antibodies (H). ALKAL1 was stained in brown. Scale bar, 10 μm. (**I**) Kaplan-Meier analysis of OS curves of melanoma patient datasets from TCGA. (**J** and **K**) Western blot analysis of phosphorylated and total MerTK proteins following simulation with (+) or without (–) IL-4/IL-13. One representative donor of eight is shown. Numbers depict the quantification of Western blot bands relative to β-actin/glyceraldehyde phosphate dehydrogenase (GAPDH). (J) BMDMs were pretreated with 50 nM siALKAL1 combined with 10 μM CH223191 or 200 μM Kyn for 48 hours. (K) MDMs were pretreated with ALKAL1 protein (1 μg/ml) combined with 10 μM CH223191 for 48 hours. Representative of three experiments. Data are means ± SEM, and *P* values were determined by two-sided Student's *t* test [(D) and (H)], one-way ANOVA [(E) and (G)], or by two-sided Wald test in a Cox-PH regression (I). $^{*}P < 0.05$, $^{**}P < 0.01$, and $^{***}P < 0.001$. Chr, chromosome.

mRNA expression of *ALKAL1* in IL-4–induced M2 macrophages (Fig. 4E). We further found that the spatial distribution of CD163, ALKAL1, and MerTK was colocalized in melanoma samples by multiplex immunofluorescence staining (Fig. 4F). In addition, our results also revealed that ALKAL1 expression was gradually increased from tumor clinicopathologic stage I to stage IV in tumor tissues of patients with melanoma (Fig. 4G). Nonresponders displayed a markedly higher expression of ALKAL1 in tumor tissues compared to that in melanoma patient responders to anti–PD-1 monoclonal antibodies (Fig. 4H). Our clinical data indicated a correlation between high ALKAL1 expression and poor patient survival across a broad range of tumors, including melanoma (Fig. 4I and fig. S6A).

To investigate whether MerTK is a responsive gene to ALKAL1, we silenced BMDMs using small interfering RNA for ALKAL1 (siALKAL1) (fig. S6, B and C). We found that the phosphorylation and expression of MerTK was repressed in IL-4–induced M2 macrophages with an ALKAL1 knockdown. In addition, CH223191 combined with siALKAL1 could further inhibit the phosphorylation and expression of MerTK in M2 macrophages, while Kyn increased these levels, providing evidence that AhR-ALKAL1 signaling could regulate the activation of MerTK (Fig. 4J). Next, human monocyte-derived macrophages (MDMs) were stimulated by IL-4 to activate ALKAL1. This led to the ligand-independent phosphorylation/activation of ALK itself (fig. S6D). Notably, the ALKAL1 protein promoted the activation and phosphorylation of MerTK after IL-4 stimulation, while CH223191 in combination with ALKAL1 protein greatly impaired this enhancement, similar to what we observed in mouse macrophages (Fig. 4K). These data suggested that ALKAL1 is the target gene of AhR and that AhR-ALKAL1 signaling regulates the activation of MerTK.

AhR-ALKAL1 signaling promotes the polarization of MerTK$^+$ macrophages to an immunosuppressive phenotype

We conducted a comprehensive investigation of the impact of AhR-ALKAL1 signaling on macrophage polarization. Initially, the expression of immunosuppressive markers was detected in IL-4–stimulated macrophages with stable siALKAL1 expression and CH223191 stimulation. Our findings demonstrated that either CH223191 or ALKAL1 silencing synergistically repressed the mRNA expression of *Arg1*, *Fizz1*, and *PD-L1* upon IL-4 stimulation (Fig. 5A). As anticipated, flow cytometry analysis revealed a reduced frequency of CD206$^+$ and Fizz1$^+$ macrophages (Fig. 5B). These results corroborated the mRNA data to indicate that the combination of CH223191 and siALKAL1 led to a substantial decrease in Arg1 protein expression compared to either CH223191 or siALKAL1 alone in IL-4–stimulated macrophages (Fig. 5C).

To further explore the effects of blocking AhR-ALKAL1 signaling on immunostimulatory phenotype polarization, we examined the expression of M1 markers in LPS-stimulated macrophages with stable ALKAL1 silencing and CH223191 stimulation. In agreement with our previous findings, CH223191 synergistically enhanced ALKAL1 silencing to promote the maximal LPS-induced expression of IL-6, IL-1β, TNF-α, and inducible nitric oxide synthase at both mRNA and protein levels (fig. S7, A to C). Concurrently, the expression of activation molecules CD86 and major histocompatibility complex–II also increased (fig. S7D). Subsequently, we evaluated the effect of CH223191-treated M2 macrophages on CD8$^+$ T cells in a coculture assay (Fig. 5D). We observed that these macrophages displayed impaired suppression of CD8$^+$ T cells upon anti-CD3/CD28 stimulation. This impairment was manifested as a reduced inhibition of CD8$^+$ T cell proliferation, along with an increased expression of activation marker CD44, and enhanced production of IFN-γ, TNF-α, perforin, and Granzyme B in CD8$^+$ T cells (Fig. 5, E to G). Collectively, our data indicated that AhR-ALKAL1 signaling promotes the polarization of macrophages to the immunosuppressive phenotype and at the same time inhibits M1 polarization to consequently suppress T cell antitumor immunity.

Specific knockout of AhR in macrophages attenuates the tumor-promoting effects of MerTK$^+$ macrophages

Given that the activation of AhR-ALKAL1 signaling enhances MerTK-mediated phagocytosis and polarization toward an immunosuppressive phenotype, we investigated whether AhR knockout could slow down the protumorigenic effects of MerTK$^+$ macrophages. To this end, AhR was deleted in a macrophage tissue–specific manner by crossing Lyz2$^{cre/+}$ with AhR$^{fl/fl}$ mice (Lyz2$^{cre/+}$Ahr$^{fl/fl}$) (Fig. 6A, and fig. S8, A and B). This macrophage-specific AhR knockout inhibited the expression of ALKAL1 and MerTK, resulting in a reduction of MerTK$^+$ macrophages (Fig. 6, B and C). Similar to the previous adoptive transfer model, MerTK$^-$ macrophages or MerTK$^+$ macrophages were isolated from tumor-bearing mice and adoptively transferred into new Ahr$^{fl/fl}$ or Lyz2$^{cre/+}$Ahr$^{fl/fl}$ recipient mice (Fig. 6D). Our findings revealed that the adoptive transfer of MerTK$^+$ macrophages into Ahr$^{fl/fl}$ and Lyz2$^{cre/+}$Ahr$^{fl/fl}$ recipient mice promotes tumor growth, whereas the presence of MerTK$^-$ macrophages did not affect tumor growth in mice. The tumor size was smaller in Lyz2$^{cre/+}$Ahr$^{fl/fl}$ mice compared to Ahr$^{fl/fl}$ mice. We further compared the tumor size after adoptive transfer of MerTK$^+$ macrophages to Ahr$^{fl/fl}$ and Lyz2$^{cre/+}$Ahr$^{fl/fl}$ recipient mice. The results indicated that the tumor size of MerTK$^+$ macrophages adoptively transferred to Lyz2$^{cre/+}$Ahr$^{fl/fl}$ mice was smaller than that transferred to Ahr$^{fl/fl}$ mice (Fig. 6, E to G). Furthermore, we investigated the immunosuppressive phenotype of macrophages and the percentage and function of effector T cells within the TME. Compared to MerTK$^-$ macrophages, MerTK$^+$ macrophages expressed higher levels of PD-L1 in both Ahr$^{fl/fl}$ and Lyz2$^{cre/+}$Ahr$^{fl/fl}$ mice (Fig. 6H). Moreover, we revealed that Lyz2$^{cre/+}$Ahr$^{fl/fl}$ mice exhibited a higher proportion of tumor-infiltrating CD8$^+$ T cells and elevated secretion of IFN-γ and TNF-α in both CD4$^+$ and CD8$^+$ T cells compared to Ahr$^{fl/fl}$ mice, irrespective of the presence or absence of adoptive transferred MerTK$^+$ macrophages (Fig. 6, I and J). As expected, decreased levels of PD-1 expression on CD4$^+$ and CD8$^+$ T cells were also observed in MerTK$^+$ macrophage adoptive transfer group of Lyz2$^{cre/+}$Ahr$^{fl/fl}$ mice (Fig. 6K). Collectively, these results suggested that specific knockout of AhR in macrophages induces immune activation within the TME, thereby attenuating the tumor-promoting effects of MerTK$^+$ macrophages.

Next, we further studied whether AhR-induced TAM reprogramming could also promote T cell antitumor reactivity in human melanoma models, using a three-dimensional (3D) human melanoma cell/TAM/T cell organoid culture (Fig. 6L). We stimulated human peripheral blood mononuclear cells (PBMCs) from healthy donors in vitro with anti-CD3/CD28 and IL-2 to expand human CD8$^+$ T cells (fig. S8C). The A375 human melanoma cells, human CD8$^+$ T cells, and IL-4/IL-13–polarized MDMs were mixed at a 2:2:1 ratio and placed in a 3D tumor organoid culture mimicking TME (Fig. 6L). IL-4/IL-13–polarized MDMs effectively suppressed

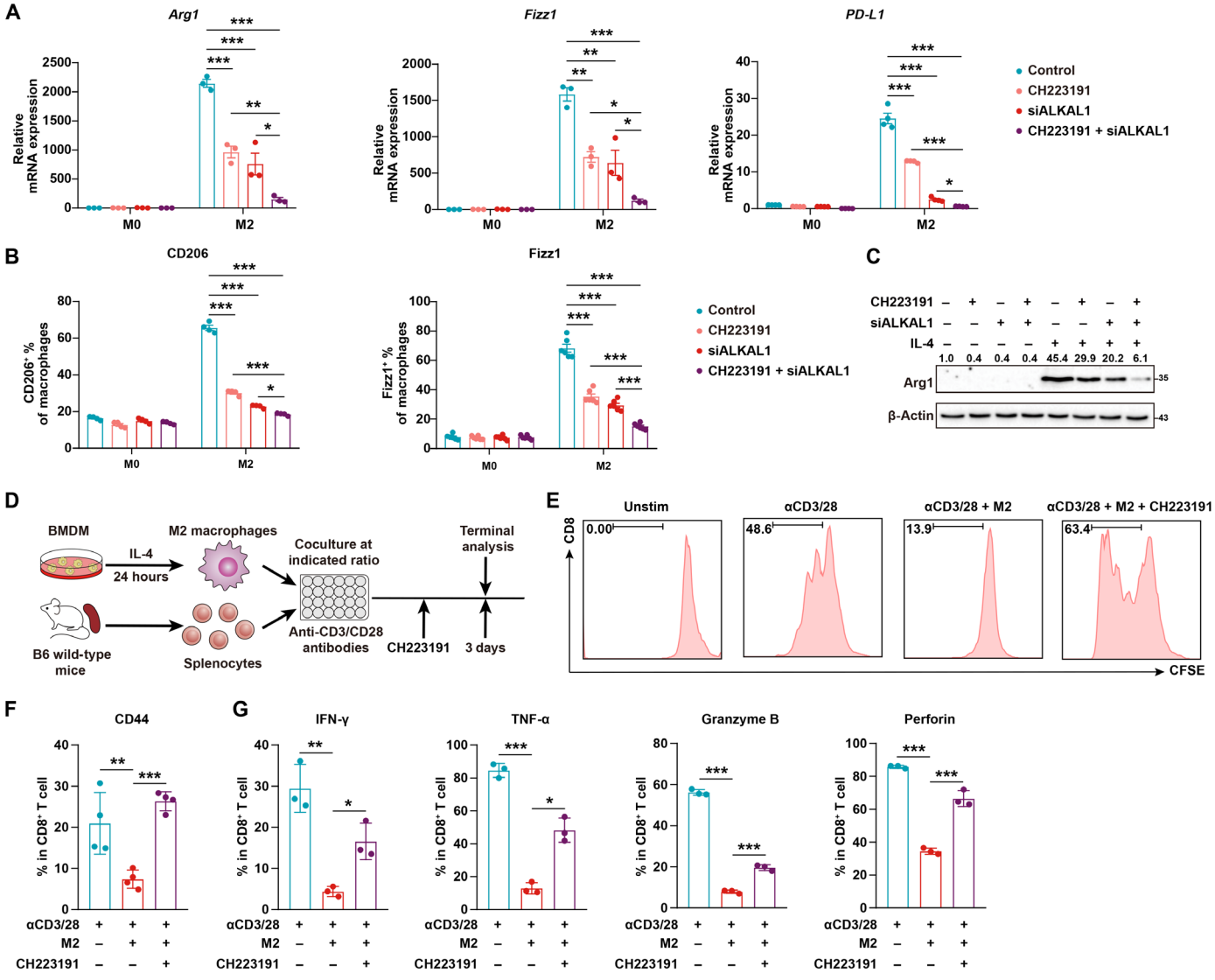

Fig. 5. AhR-ALKAL1 signaling promotes the polarization of MerTK$^+$ macrophages to immunosuppressive phenotype. (**A** to **C**) BMDMs were pretreated with 50 nM siALKAL1 combined with 10 μM CH223191 and/or IL-4 (20 ng/ml) for 48 hours during polarization of macrophages. (A) RT-PCR analysis of M2 marker *Arg1*, *Fizz1*, and *PD-L1* mRNA expression. (B) Flow cytometry analysis of the percentages of macrophages expressing CD206 and Fizz1. (C) Western blot analysis of Arg1 protein levels. One representative donor of eight is shown. Numbers depict the quantification of Western blot bands relative to β-actin. (**D** to **G**) Studying the T cell suppression function of CH223191-treated and IL-4–polarized BMDMs in an in vitro macrophage/T cell coculture assay. (D) Experimental design. (E) Carboxyfluorescein diacetate succinimidyl ester (CFSE)–labeled splenocytes were cocultured with IL-4–polarized BMDMs for 3 days. Flow cytometry analysis of CFSE dilution and CD8$^+$ T cell divisions. [(F) and (G)] Flow cytometry analysis of the percentage of CD44 (F), IFN-γ, TNF-α, Granzyme B, and perforin (G) in CD8$^+$ T cells. Representative of three experiments. Data are means ± SEM, and *P* values were determined by two-way ANOVA [(A) and (B)] or by one-way ANOVA [(F) and (G)]. **P* < 0.05, ***P* < 0.01, and ****P* < 0.001.

T cell–mediated killing of A375 tumor cells; this immunosuppressive effect was largely alleviated by CH223191 treatment during MDM polarization (Fig. 6M). Accordingly, human CD8$^+$ T cells cocultured with CH223191-treated MDMs, compared to those cocultured with non–CH223191-treated MDMs, showed an enhancement in T cell activation, as evidenced by increased expression of CD69 and enhanced production of IFN-γ and TNF-α in CD8$^+$ T cells (Fig. 6, N and O). Collectively, these data suggest that CH223191-induced human TAMs reprogramming has the potential to improve antitumor T cell responses.

Targeting TAMs by AhR inhibition prevents tumor growth and enhances aPD-L1 efficacy

Our findings had so far indicated that AhR plays a critical role in regulating MerTK-mediated phagocytosis and the polarization of immunosuppressive macrophages, thereby promoting tumor progression. To evaluate whether we could exploit this knowledge for cancer immunotherapy, we developed a nanocarrier for delivery of the AhR antagonist CH223191, using mannosylated micelles (CH223191-MMic) that specifically target MerTK$^+$ macrophages through CD206 (fig. S9, A and B).

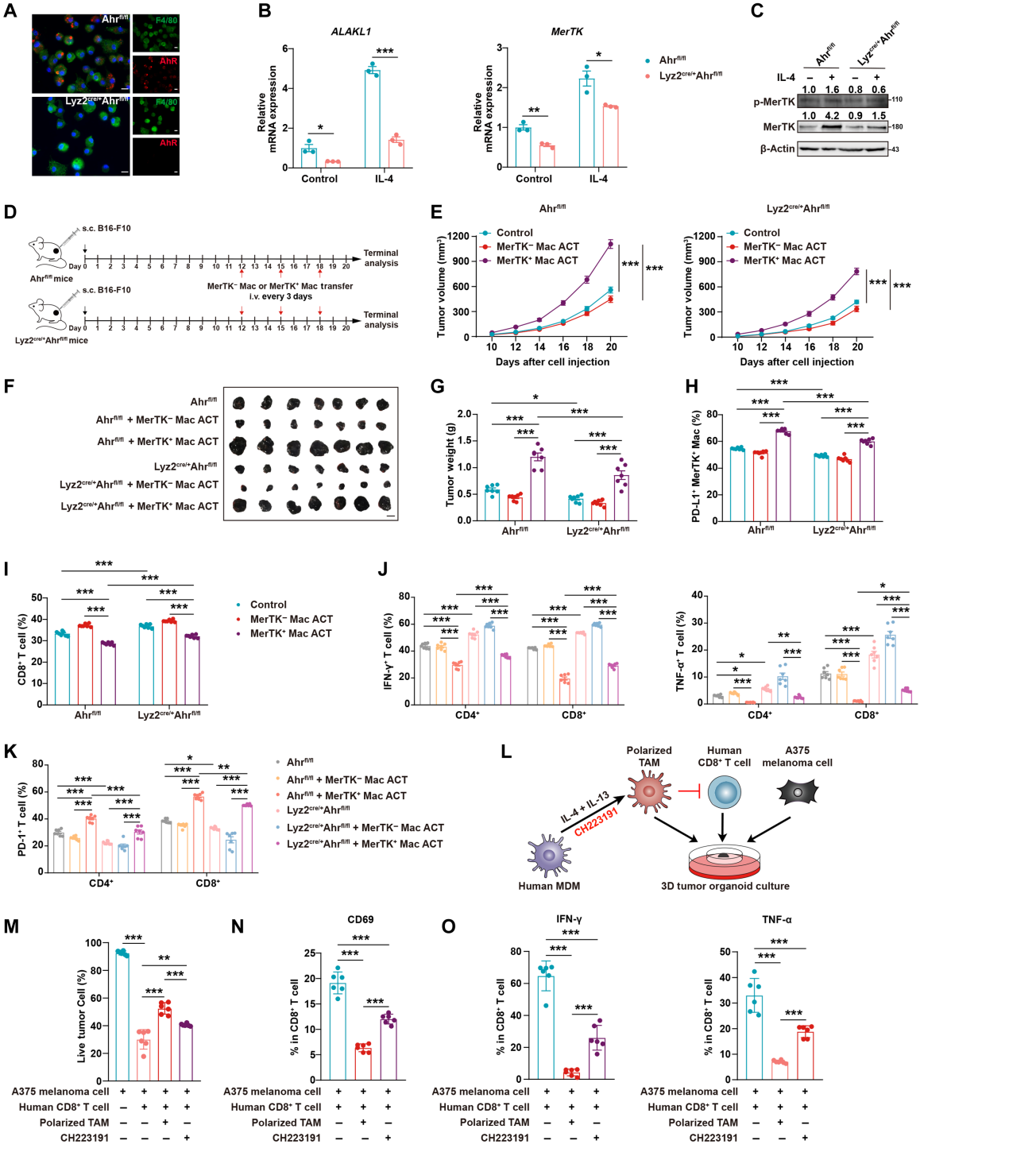

Fig. 6. Specific knockout of AhR in macrophages attenuates the tumor-promoting effects of MerTK$^+$ macrophages. (**A**) Representative combined staining of F4/80 (green) and AhR (red) in BMDMs of the indicated genotype. DAPI (blue) was the nuclear stain. Scale bar, 10 μm. (**B**) RT-PCR analysis of *ALKAL1* and *MerTK* mRNA expression in BMDMs of the indicated genotype. (**C**) Western blot analysis of phosphorylated and total MerTK proteins with (+) or without (−) IL-4 polarization in BMDMs of the indicated genotype for 24 hours. One representative donor of four is shown. Numbers depict the quantification of Western blot bands relative to β-actin. (**D** to **K**) Studying the effect of MerTK$^+$ Mac in a Lyz$^{cre/+}$Ahr$^{fl/fl}$ B16-F10 syngeneic mouse tumor model. (D) Adoptive transfer method. (E) Tumor growth. (F) Subcutaneous B16-F10 tumors were surgically removed and presented. Scale bar, 1 cm. (G) Tumor weight. (H) Flow cytometry analysis of the percentages of PD-L1$^+$ cells in MerTK$^+$ Mac. (I) Flow cytometry analysis of the percentages of CD8$^+$ T cells in CD3$^+$ T cells. [(J) and (K)] Flow cytometry analysis of the percentages of cells expressing IFN-γ and TNF-α (J) and PD-1 (K) in CD4$^+$ and CD8$^+$ T cells. (**L**) Experimental design. (**M**) Flow cytometry analysis of the percentage of live tumor cells (gated as hCD3$^-$hCD114$^-$annexin V$^-$PI$^-$ cells). (**N** and **O**) Flow cytometry analysis of the percentage of CD69 (N), IFN-γ and TNF-α (O) in CD8$^+$ T cells. Representative of three experiments. Data are means ± SEM, and *P* values were determined by two-way ANOVA [(B) and (G) to (K)] or by one-way ANOVA [(E) and (M) to (O)]. **P* < 0.05, ***P* < 0.01, and ****P* < 0.001.

We characterized the CH223191-MMic formulation and confirmed its suitability for biomedical applications. Transmission electron microscopy (TEM) images revealed the spherical morphology of the micelles, with an average size of approximately 100 nm (Fig. 7A). Dynamic light scattering analysis indicated an average hydrodynamic diameter of 106 nm, slightly larger than the TEM measurements, and demonstrated a uniform shape and narrow size distribution of the micelles with a negative surface charge of −27.68 ± 0.88 mV (Fig. 7, B and C). The release of CH223191 from the micelles was relatively rapid initially, reaching a 60% cumulative release after 12 hours due to partial damage to the micelle coating. Further release was subsequently observed with an increase in incubation time (Fig. 7D). We also confirmed the efficient uptake of Cy3-labeled CH223191-MMic by macrophages after coincubation for 6 hours (Fig. 7E). The biocompatibility of CH223191-MMic was assessed to ensure safe application for biomedical purposes. Cytotoxicity studies using the Cell Counting Kit-8 (CCK-8) assay on B16-F10 cells showed that even at a high concentration of 100 μg/ml, CH223191-MMic did not induce significant toxicity, with cell viability remaining above 90% after 24 and 48 hours of incubation (Fig. 7F). Live fluorescence imaging in tumor-bearing mice revealed efficient accumulation and selective targeting of MMic at the tumor site as early as 2 hours after injection, with a peak intensity reached at 24 hours. Limited fluorescence was observed in other organs, including the heart, liver, spleen, lung, and kidney, indicating that MMic accumulated mainly at the tumor site and were gradually metabolized thereafter (Fig. 7G). On the basis of this information, the MMic were administered every 3 days in subsequent experiments (Fig. 7H). An in vivo biocompatibility evaluation of CH223191-MMic showed normal hepatic and renal function, as evidenced by serum biochemical markers within the normal range, with no pathological changes in the normal organs being observed (fig. S9, C to E). These results collectively indicated the safety of using CH223191-MMic as a potential melanoma therapy.

To next evaluate the treatment effects of CH223191-MMic, we established a B16-F10 xenograft melanoma model and treated it with saline, free CH223191, MMic, or CH223191-MMic by intravenous injection. CH223191 was used at the dose of 0.5 mg/kg on days 12, 15, and 18 (Fig. 7H). Tumor size measurements was used to evaluate the treatment effects. The CH223191-MMic–treated group exhibited significant tumor suppression in terms of tumor volume and weight (Fig. 7, I to K). We tested for a potential effect of CH223191-MMic. To gain insights into the immunotherapeutic mechanism of CH223191-MMic, we examined multiple cell subsets within the TME. We observed that MerTK$^+$ macrophages and their expressed PD-L1 levels were reduced in the CH223191-MMic group (Fig. 7, L and M), which was consistent with our conclusion above that AhR regulated the expression of MerTK$^+$ macrophages. Consistently, the CH223191-MMic–treated group also displayed higher percentages of CD8$^+$ T cells and increased percentages of IFN-γ$^+$ and TNF-α$^+$ CD4$^+$ and CD8$^+$ T cells, along with decreased PD-1 expression (Fig. 7, N to P). These results suggested that targeting TAMs with CH223191-MMic enhances the antitumor immune response. Survival curves indicated that 50% of the mice of the intratumor injection of CH223191-MMic group survived for more than 38 days, which is substantially higher than the survival rate of the control groups (Fig. 7Q).

We further evaluated the potential of CH223191-MMic as a partner in the combination therapy, particularly conjunction with other ICB therapies, such as a PD-1/PD-L1 blockade therapy (Fig. 8A). Although most ICB therapies target CD8$^+$ T cells, these cells are closely regulated by TAMs in the TME, thus making TAMs targeting another potential avenue for immunotherapy (*31*, *32*). In B16-F10 xenograft melanoma, the administration of either CH223191-MMic or aPD-L1 treatment alone suppressed the progression of preestablished solid tumors at a level comparable to the control treatment. Combining aPD-L1 and CH223191-MMic resulted in the strongest effect, yielding synergistic tumor suppression efficacy compared with either therapy alone (Fig. 8, B to D). Treatment of both CH223191-MMic and PD-L1 blockade alone decreased the proportions of MerTK$^+$ macrophages; however, in the combined treatment group, there was less of an immunosuppressive phenotype of macrophages (Fig. 8E). Furthermore, the combined CH223191-MMic and PD-L1 blockade treatment led to increased infiltration of activated CD8$^+$ T cells (Fig. 8F). Intratumoral IFN-γ$^+$ and TNF-α$^+$ CD4$^+$ and CD8$^+$ T cells increased in the combination therapy group compared with either therapy alone (Fig. 8G). We further tested for a potential effect of dual CH223191-MMic and PD-L1 blockade. Control mice [isotype immunoglobulin G (IgG)–treated] had a median survival of 24 days (Fig. 8H). Administration of either aPD-L1 IgG alone increased survival; however, combining aPD-L1 IgG and CH223191-MMic had the strongest effect by extending the survival twofold compared with the control treatment and by increasing the survival up to 20% higher than either therapy alone (Fig. 8H). Together, these data provide a proof of principle for the cancer immunotherapy potential of AhR inhibition via targeting MerTK$^+$ macrophages, thereby enhancing aPD-L1 efficacy.

DISCUSSION

Despite our increasing understanding of macrophage heterogeneity, drivers of macrophage phenotypic and functional polarization in the microenvironment are not fully elucidated (*33*). Here, we identified a unique subpopulation of tumor-permissive macrophages expressing high levels of MerTK by scRNA-seq and unveiled the regulatory role of AhR-ALKAL1 signaling in MerTK-mediated phagocytosis, which is known to exacerbate tumor progression (fig. S10). Emerging studies indicate that TAMs can coexist within the same tumor as immunostimulatory and immunosuppressive subtypes (*34*, *35*). On the basis of our current findings, MerTK$^+$ macrophages constitute a distinct subset of TAMs infiltrating the TME and act as immunosuppressive controllers, shaping an immunoevasive contexture in melanoma. Therapeutically targeting immunosuppressive MerTK$^+$ macrophages holds great promise to improve current treatment options for patients with melanoma.

In our study, enhancement of antitumor immunity in a mouse model is achieved by targeting MerTK$^+$ macrophages with AhR antagonist. Prior reports that AhR is both protumorigenic and a tumor suppressor suggests that an efficacious AhR ligand may not exhibit a "one-size-fits-all" role for limiting different types of cancer (*36*). In addition, macrophage AhR function promotes the expression of Arg1 and IL-10 in TAMs and inhibits IFN-γ expression in CD8$^+$ T cells in both pancreatic cancer and glioblastoma (*31*, *37*), which is consistent with our conclusion that the specific knockout of AhR in macrophages resulted in slowed tumor growth in melanoma. Moreover, the abundance of MerTK$^+$ macrophages in the TME negatively correlated with the levels of CD8$^+$ T cell infiltration and the effector functions of CD8$^+$ T cells, signifying a highly immunosuppressive state. However, immune effector cells presented

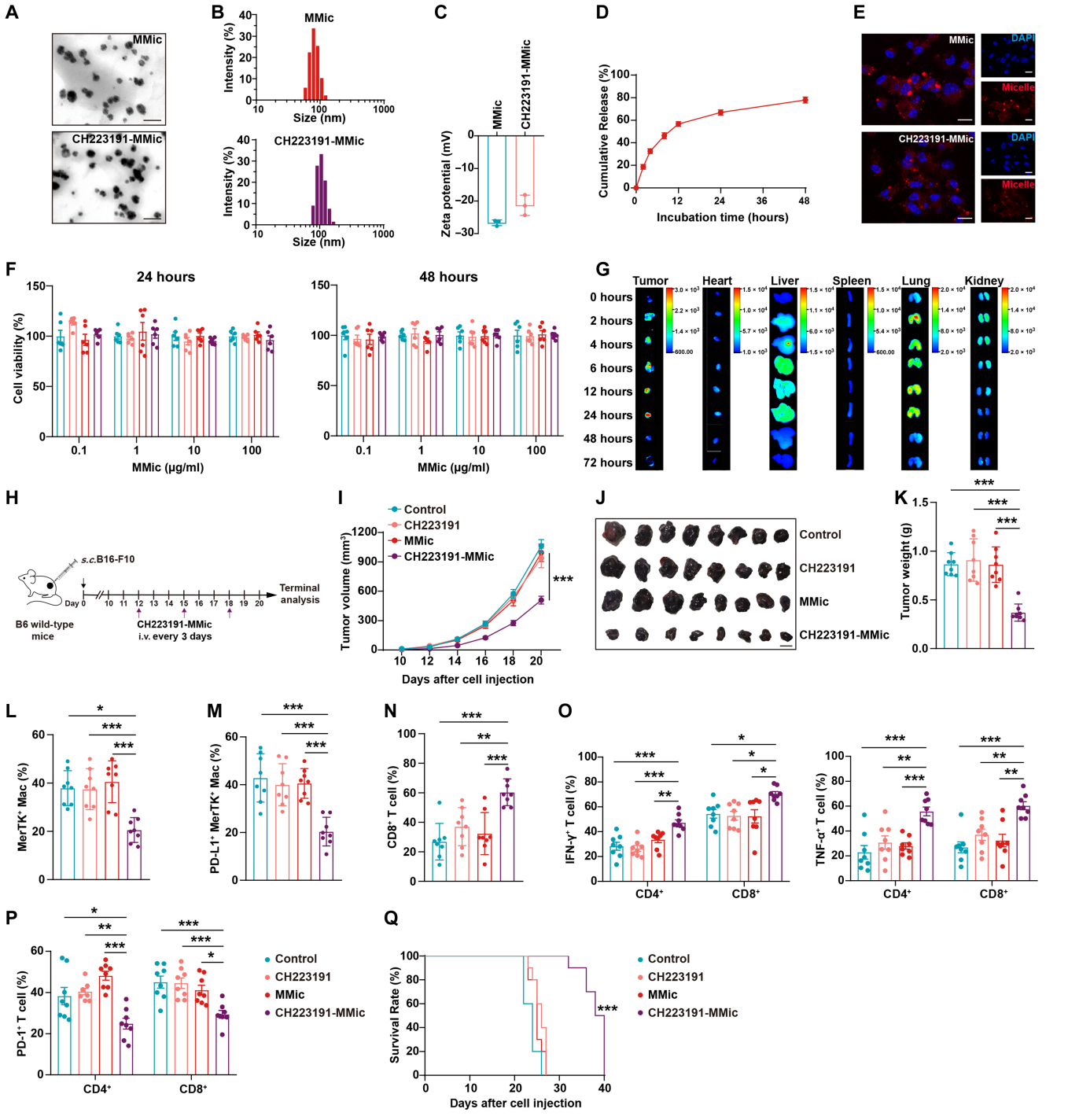

Fig. 7. Targeting TAMs by AhR inhibition prevents tumor growth. (**A** to **E**) Characteristics of the prepared CH223191-MMic. (A) TEM images of MMic and CH223191-MMic. Scale bar, 100 nm. (B) Size and size distributions of MMic and CH223191-MMic. (C) Zeta potential of MMic and CH223191-MMic. (D) Cumulative CH223191 release profile of CH223191-MMic. (E) Shown are representative confocal images of BMDMs engulfing micelles (red) for 6 hours. DAPI (blue) was the nuclear counterstain. Scale bar, 10 μm. (**F**) CCK8 analysis of the cell viabilities of B16-F10 cells treated with various concentrations of MMic for 24 or 48 hours. (**G**) Fluorescence imaging of ex vivo major organs from tumor-bearing mice treated with Cy7-labeled CH223191-MMic after various time periods. (**H** to **Q**) Studying the cancer immunotherapy potential of CH223191-MMic treatment in a B16-F10 syngeneic mouse tumor model. (H) Experimental design. (I) Tumor growth. (J) Subcutaneous B16-F10 tumors were surgically removed and presented. Scale bar, 1 cm. (K) Tumor weight. (L) Flow cytometric analysis of the percentages of MerTK$^+$ Mac in B16-F10 tumors at day 20 after implantation. (M) Flow cytometry analysis of the percentages of PD-L1$^+$ cells in MerTK$^+$ Mac. (N) Flow cytometry analysis of the percentages of CD8$^+$ T cells in CD3$^+$ T cells. [(O) and (P)] Flow cytometry analysis of the percentages of cells expressing IFN-γ and TNF-α (O) and PD-1 (P) in CD4$^+$ and CD8$^+$ T cells. (Q) Survival curves of mice treated with saline, free CH223191, MMic, or CH223191-MMic. Representative of three experiments. Data are the means ± SEM, and *P* values were determined by one-way ANOVA [(I) and (K) to (N)], two-way ANOVA [(O) and (P)] or by log-rank test (Q). *$P < 0.05$, **$P < 0.01$, and ***$P < 0.001$.

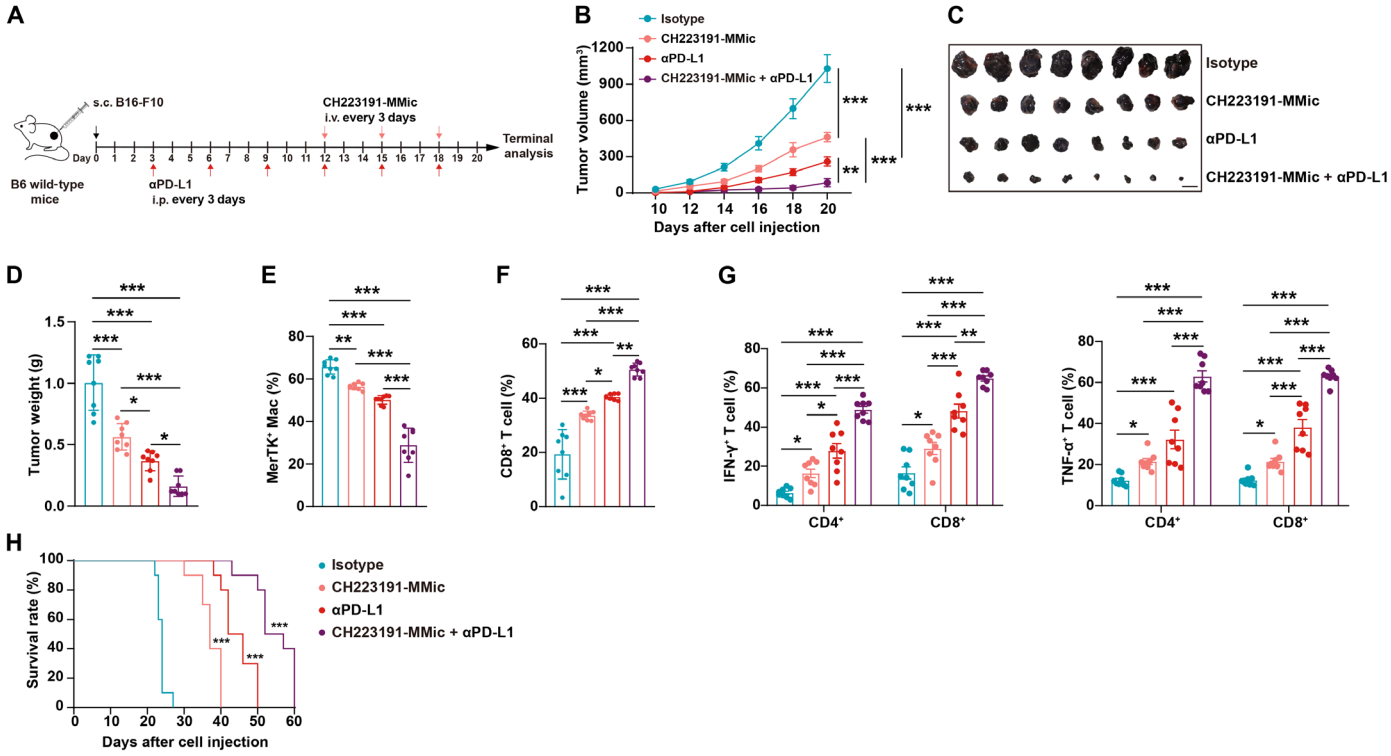

Fig. 8. Targeting TAMs by AhR inhibition enhances aPD-L1 efficacy. [(A) to (H)] Studying the cancer immunotherapy potential of CH223191-MMic and aPD-L1 treatment in a B16-F10 syngeneic mouse tumor model. (**A**) Experimental design. (**B**) Tumor growth. (**C**) Subcutaneous B16-F10 tumors were surgically removed and presented. Scale bar, 1 cm. (**D**) Tumor weight. (**E**) Flow cytometric analysis of the percentages of MerTK$^+$ Mac in B16-F10 tumors at day 20 after implantation. (**F**) Flow cytometry analysis of the percentages of CD8$^+$ T cells in CD3$^+$ T cells. (**G**) Flow cytometry analysis of the percentages of cells expressing IFN-γ and TNF-α in CD4$^+$ and CD8$^+$ T cells. (**H**) Survival curves of mice treated with CH223191-MMic, aPD-L1 blockade, or a combination of the two versus controls. Representative of three experiments. Data are mean values ± SEM, and *P* values were determined by one-way ANOVA [(B) and (D) to (F)], two-way ANOVA (G), or by log-rank test (H). **P* < 0.05, ***P* < 0.01, and ****P* < 0.001.

an exhausted or dysfunctional state and, therefore, could not play an active role in antitumor immunity.

Traditionally, nuclear receptors such as liver X receptor (LXR), peroxisome proliferator–activated receptor γ (PPARγ), and nuclear receptor subfamily 4 group A member 2 (Nr4a2) have been recognized as key players at the interface of inflammation and metabolic signaling in the context of efferocytosis (*38*, *39*). Upon ligand binding, they repress the transcription of inflammatory genes while increasing the expression of MerTK (*38*, *40*, *41*). In vivo and ex vivo studies have demonstrated impaired phagocytic clearance in mice lacking LXRαβ, PPARδ, or RXRα (*42*). In addition, AhR, PPARγ, and LXR are nuclear transcription factors. Studies in aggressive tumors and tumor cell lines have revealed elevated levels of AhR with constitutive nuclear localization (*36*), but its regulation of MerTK expression has remained unclear. Previous research has indicated that apoptotic cell death exposes DNA, leading to a Toll-like receptor 9–dependent activation of AhR and downstream immune suppression and tolerance, thus limiting disease severity in lupus-prone mice (*43*). Building upon this knowledge, we further revealed herein that our study brings different understandings of innate immune resistance mechanism and suggests that targeting AhR-ALKAL1-MerTK signaling in melanoma could represent a promising treatment option, especially in overcoming immunotherapeutic tolerance. These findings unveil a previously unknown role for AhR-ALKAL1-MerTK signaling in the regulation of MerTK$^+$ macrophages phenotype and function by melanoma.

Our ChIP-seq analysis suggested that ALKAL1, a physiological ligand of ALK and LTK (*44*), is one of the direct targets of AhR. Together with the activating cytokines ALKAL2 and ALKAL1, they play roles in neural development, cancer, and autoimmune diseases (*45*–*47*). ALKAL1 and ALKAL2 share highly similar structures, with an N-terminal variable region and a conserved C-terminal augmentor domain, both capable of stimulating ALK phosphorylation activity to a level similar to full-length ALKAL1 (*28*–*30*). Because MerTK and ALK belong to the same family of RTKs, we hypothesized that ALKAL1 may bind to the phagocytosis receptor MerTK to stimulate MerTK phosphorylation and activation. Our current results confirmed that ALKAL1 promoted MerTK phosphorylation, which led to the enhanced phagocytosis in MerTK$^+$ macrophages. In addition, the up-regulation of ALKAL1 was identified and correlated with tumor malignancy and a poor prognosis in patients with various tumors, including melanoma.

Compared to many new therapeutic candidates, MerTK is unique in that it is already an established drug target because of its known functions in tumors. Small-molecule MerTK inhibitors have been developed for the combination therapy with osimertinib in *EGFR*-mutant non–small cell lung cancer, which has shown efficacy in reversing osimertinib resistance during human phase 1 trials (ClinicalTrials.gov, NCT04762199) (*26*). In addition, MerTK signaling acts as an innate immune checkpoint (*48*, *49*). In this present study, we have elucidated the enrichment of MerTK as a target in the TME infiltrated with TAMs, highlighting its role as an innate

immune resistance mechanism following unsuccessful anti–PD-1 therapy. Consequently, our findings offer mechanistic insights for patient stratification and selection of combination therapies targeting both MerTK and PD-1 or PD-L1.

MATERIALS AND METHODS

Key resources

Reagent information is listed in Table 2.

Mice

Female C57BL/6 wild-type mice (6 to 8 weeks) were purchased from Beijing Huafukang Bioscience Co. Inc. AhR-floxed mice were generated by Cyagen Biosciences Inc. Briefly, guide RNA targeting the mouse AhR gene, the donor vector containing loxP sites flanking exons 5, 6, and 7 of the AhR gene, and Cas9 mRNA were coinjected into fertilized mouse eggs to generate targeted conditional knockout mice. F_0 founder animals were identified by PCR followed by sequence analysis. Positive offspring were then bred to wild-type mice to test germline transmission and F_1 animal generation. F_1 mice were bred with wild-type mice to generate more positive F_2 animals, which were identified by PCR. AhR-floxed hemizygous mice were bred to generate homozygous offspring, which were then crossed with Lyz2-Cre hemizygous mice to specifically target AhR expression on all hematopoietic cells. AhR-floxed homozygous Lyz2-Cre–negative littermates were used as controls. All mice were bred under specific pathogen–free conditions. All animal procedures were performed in compliance with protocols approved by the Hubei Provincial Animal Care and Use Committee, following the experimental guidelines of the Animal Experimentation Ethics Committee of the Huazhong University of Science and Technology (HUST, approval no. IACUC-3221).

Cell lines

Mouse B16-F10 cells were obtained from the American Type Culture Collection and cultured in Dulbecco's modified Eagle's medium (DMEM) containing 10% fetal bovine serum (FBS) and penicillin/streptomycin (100 U/ml; Gibco).

Human specimens

Fresh tumor tissue samples from patients with melanoma were surgically resected and obtained with informed consent under a protocol approved by HUST (Wuhan, China). We strictly adhered to all relevant ethical regulations. For the multicolor immunohistochemical staining and scRNA-seq, samples from patients with melanoma were also surgically resected and obtained with informed consent under a protocol approved by the Union Hospital, Tongji Medical College ethics committee (HUST, approval no. [2023]0489-01). Tables S1 and S2 provide information about the sex, age, and tumor characteristics of the patients.

Tissue handling and tumor disaggregation

Resected tumors were immediately transported in DMEM on ice after surgical procurement and rinsed with PBS. The tumor was minced into tiny cubes <1 mm^3 using scalpels and transferred into a 50-ml conical tube containing 10-ml prewarmed M199 media (Gibco), collagenase P (2 mg/ml; Roche), and deoxyribonuclease I (DNase I) (10 U/μl; Roche). Tumor pieces were digested in this digestion media and vortexed at 250 rpm for 2 hours at 37°C. If necessary, this process was repeated twice more until a single-cell suspension was obtained. The resulting suspension was then filtered using a 70-μm nylon mesh, and any residual cell clumps were discarded. The suspension was supplemented with 30 ml of PBS with 2% FBS (Gibco) and immediately placed on ice. After centrifuging at 580*g* at 4°C for 6 min, the supernatant was discarded, and the cell pellet was resuspended in PBS with FBS and placed on ice before staining for FACS.

Single-cell RNA sequencing

Single-cell suspensions were stained for 30 min using an antibody against CD45-PerCP-Cy5.5 (eBioscience). Propidium iodide (PI) (eBioscience) was freshly added before cell sorting. $CD45^+PI^-$ single cells were sorted for library construction of scRNA-seq. The libraries were prepared using the Chromium Next GEM Single Cell 3′ GEM, Library & Gel Bead Kit v3.1 (catalog no. 1000128) purchased from 10x Genomics following the manufacturer's protocols. The target cell recovery for each library was aimed to be 8000, and the libraries were sequenced on an Illumina HiSeq X Ten platform.

scRNA-seq analysis

10x Genomics scRNA-seq data were aligned and quantified using the Cell Ranger Single-Cell Software Suit (version 6.0.1) against the mm10 reference genome. The quality filtering on scRNA-seq data was performed by multiple filtering parameters including filtering out cells with >20% of mitochondrial genes and lower genes expression capture (<200 or >8000 genes), and genes only uniquely expressed in <3 cells in the dataset. In addition, we applied DoubletFinder (version1.1.8) to identify doublets with 15 principal components and default threshold (*50*). We normalize the count data using the function NormalizeData built in the R package Seruat (version 3.2.3) (*51*). To cluster single cells by their expression, the unsupervised graph-based clustering algorithm implemented in Seurat R package (version 3.2.3) was used for each dataset. Top 2000 variable genes identified by vst method were used to perform principal components analysis. One to 20 principal components were used in FindNeighbors function. The FindClusters function was used to determine the clusters (*52*). To identify subsets within myeloid cells, we further performed clustering for those cells.

To identify the differentially expressed genes (DEGs) in different clusters or groups, we performed differential expression analysis. These DEGs or cluster-specific biomarkers were obtained using the FindAllMarkers (*53*) function with default parameters and the following thresholds: at least 0.25-fold difference (log scale) between the two groups of cells, minimum fraction of genes expressing in both clusters >0.2, and only return positive markers.

On the basis of these DEGs, enriched gene ontology terms or KEGG (Kyoto Encyclopedia of Genes and Genomes) were acquired for each subcluster or group using the cluster Profiler package (version 3.18.1) (*54*) with default parameters. Annotation Database was performed to map these DEGs,and the visualization was shown by bar plot. The information on cell types was provided in tables S3 and S4.

Ligand and receptor interaction analysis

To identify the significant and specific ligand-receptor pairs between macrophage and $CD8^+$ T cell subtypes, the CellChat was used in our scRNA-seq data (*55*). Ligand-receptor pairs with a *P* value of less than 0.05 determined by CellChat were considered to be significant interacting molecules between different cell subpopulations.

Table 2. Reagent information. N/A, not applicable.

Reagent	Source	Identifier
Antibodies		
TruStain FcX (anti-mouse CD16/32) Antibody	BioLegend	Catalog no. 101320; RRID: AB_1574975
Brilliant Violet 510 anti-mouse CD45 Antibody	BioLegend	Catalog no. 103138; RRID: AB_2563061
CD45 Monoclonal Antibody (HI30), PerCP-Cyanine5.5	eBioscience	Catalog no. 45-0459-41; RRID: AB_10718244
PerCP/Cyanine5.5 anti-mouse CD11c Antibody	BioLegend	Catalog no. 117328; RRID: AB_2129641
PE/Dazzle 594 anti-mouse/human CD11b Antibody	BioLegend	Catalog no. 101256; RRID: AB_2563648
Brilliant Violet 421 anti-mouse F4/80 Antibody	BioLegend	Catalog no. 123132; RRID: AB_11203717
APC anti-mouse Ly-6C Antibody	BioLegend	Catalog no. 128016; RRID: AB_1732076
PE/Cyanine7 anti-mouse Ly-6G Antibody	BioLegend	Catalog no. 127618; RRID: AB_1877261
BV421 Hamster Anti-Mouse CD80	BD Horizon	Catalog no. 562611; RRID: AB_2737675
APC anti-mouse CD86 Antibody	BioLegend	Catalog no. 105012; RRID: AB_493342
Alexa Fluor 488 anti-mouse I-A/I-E Antibody	BioLegend	Catalog no. 107616; RRID: AB_493523
PE anti-mouse CD206 (MMR) Antibody	BioLegend	Catalog no. 141706; RRID: AB_10895754
FITC anti-mouse CD3 Antibody	BioLegend	Catalog no. 100204; RRID: AB_312661
Alexa Fluor 700 anti-mouse CD4 Antibody	BioLegend	Catalog no. 100430; RRID: AB_493699
Brilliant Violet 605 anti-mouse CD8a Antibody	BioLegend	Catalog no. 100743; RRID: AB_2561352
PerCP anti-mouse/human CD44 Antibody	BioLegend	Catalog no. 103036; RRID: AB_10645506
Brilliant Violet 750 anti-mouse TNF-α Antibody	BioLegend	Catalog no. 506358; RRID: AB_2801090
Brilliant Violet 650 anti-mouse IFN-γ Antibody	BioLegend	Catalog no. 505832; RRID: AB_2734492
PE anti-human/mouse Granzyme B Recombinant Antibody	BioLegend	Catalog no. 372208; RRID: AB_2687032
APC anti-mouse Perforin Antibody	BioLegend	Catalog no. 154304; RRID: AB_2721463
PerCP/Cyanine5.5 anti-mouse/human CD45R/B220 Antibody	BioLegend	Catalog no. 103236; RRID: AB_893354
PE/Cyanine7 anti-mouse NK-1.1 Antibody	BioLegend	Catalog no. 108714; RRID: AB_389364
PE/Dazzle 594 anti-mouse CD279 (PD-1) Antibody	BioLegend	Catalog no. 135228; RRID: AB_2566006
Brilliant Violet 605 anti-mouse CD274 (B7-H1, PD-L1) Antibody	BioLegend	Catalog no. 124321; RRID: AB_2563635
PE anti-mouse CD274 (B7-H1, PD-L1) Antibody	BioLegend	Catalog no. 124308; RRID: AB_2073556
Brilliant Violet 421 anti-mouse MERTK (Mer) Antibody	BioLegend	Catalog no. 151510; RRID: AB_2832533
Brilliant Violet 711 anti-mouse MERTK (Mer) Antibody	BioLegend	Catalog no. 151515; RRID: AB_2876505
Brilliant Violet 605 anti-human CD45 Antibody	BioLegend	Catalog no. 304042; RRID: AB_2562106
FITC anti-human CD14 Antibody	BioLegend	Catalog no. 325617; RRID: AB_2571928
PE/Cyanine7 anti-human CD14 Antibody	BioLegend	Catalog no. 367115; RRID: AB_830690
FITC anti-human CD3	BioLegend	Catalog no. 300306; RRID: AB_314042
PerCP/Cyanine5.5 anti-human CD8a	BioLegend	Catalog no. 301032; RRID: AB_893422
Brilliant Violet 421 anti-human CD69 Antibody	BioLegend	Catalog no. 310930; RRID: AB_2561909
PE anti-human IFN-γ Antibody	BioLegend	Catalog no. 502509; RRID: AB_315234
APC anti-human TNF-α Antibody	BioLegend	Catalog no. 502912; RRID: AB_315264
Ultra-LEAF Purified anti-human CD3 Antibody	BioLegend	Catalog no. 317326; RRID: AB_11150592
Ultra-LEAF Purified anti-human CD28 Antibody	BioLegend	Catalog no. 302934; RRID: AB_11148949
CD3e Monoclonal Antibody, Functional Grade	eBioscience	Catalog no. 16-0031-85; RRID: AB_468848
CD28 Monoclonal Antibody, Functional Grade	eBioscience	Catalog no. 16-0281-85; RRID: AB_468922
AHR Monoclonal Antibody (RPT9)	Thermo Fisher Scientific	Catalog no. MA1513; RRID: AB_2223958
FAM150A Polyclonal Antibody	Thermo Fisher Scientific	Catalog no. PA5-55591; RRID: AB_2641273
Ah Receptor (A-3)	Santa Cruz Biotechnology	Catalog no. sc-133088
NOS2 (M-19)	Santa Cruz Biotechnology	Catalog no. sc-650

(Continued)

(Continued)

Reagent	Source	Identifier
Arginase-1 Polyclonal antibody	Proteintech	Catalog no. 16001-1-AP
Beta Actin Monoclonal antibody	Proteintech	Catalog no. 66009-1-Ig
Aryl hydrocarbon receptor polyclonal antibody	Enzo Life	Catalog no. BML-SA210-0100
Mouse Mer Antibody	R&D Systems	Catalog no. AF591
Mouse MMR/CD206 Antibody	R&D Systems	Catalog no. AF2535
F4/80 (D2S9R) XP Rabbit mAb	Cell Signaling Technology	Catalog no. 70076S
ALK (D5F3) XP Rabbit mAb	Cell Signaling Technology	Catalog no. 3633
Phospho-ALK (Tyr1604) Antibody	Cell Signaling Technology	Catalog no. 3341
Anti-CD163 antibody	Abcam	Catalog no. ab182422
Anti-MERTK (phospho Y749) + TYRO3 (phospho Y681) antibody	Abcam	Catalog no. ab192649
Anti-MERTK antibody [Y323]	Abcam	Catalog no. ab52968
Mouse IgG3, kappa monoclonal [MG3-35] -	Abcam	Catalog no. ab18394
Anti-CD3 antibody	Abcam	Catalog no. ab16669
Anti-CD4 antibody	Abcam	Catalog no. ab133616
Anti-CD8 antibody	Abcam	Catalog no. ab237709
Anti-CD69 antibody	Abcam	Catalog no. ab233396
Anti-CD103 antibody	Abcam	Catalog no. ab129202
Goat Anti-Rabbit IgG H&L (Alexa Fluor 594) preadsorbed	Abcam	Catalog no. ab150084
Goat Anti-Rabbit IgG H&L (Alexa Fluor 488) preadsorbed	Abcam	Catalog no. ab150081
Goat Anti-Mouse IgG H&L (Alexa Fluor 488)	Abcam	Catalog no. ab150113
Goat Anti-Mouse IgG H&L (Cy3) preadsorbed	Abcam	Catalog no. ab97035
InVivoMab anti-mouse PD-L1 (B7-H1)	Bio X Cell	Catalog no. BE0101; RRID: AB_10949073
InVivoPlus rat IgG2a isotype control, antitrinitrophenol	Bio X Cell	Catalog no. BP0090; RRID: AB_1107769
GAPDH Rabbit mAb	ABclonal	Catalog no. A19056
Chemicals, peptides, and recombinant proteins		
LPS-EB Ultrapure	InvivoGen	Catalog no. tlrl-3pelps
Recombinant Murine IL-4	PeproTech	Catalog no. 214-14-20
Recombinant Human M-CSF	PeproTech	Catalog no. 300-25
Recombinant Human IL-2	PeproTech	Catalog no. 200-02
Recombinant Human IL-4 (carrier-free)	BioLegend	Catalog no. 574004
Recombinant Human IL-13 (carrier-free)	BioLegend	Catalog no. 571104
IL2 Protein, Mouse, Recombinant	Sino Biological	Catalog no. 51061-MNAE
Recombinant Mouse M-CSF Protein	R&D Systems	Catalog no. 416-ML-050
ALKAL1 Protein, Human (His, B2M)	MCE	Catalog no. HY-P71584
L-Kynurenine	Sigma-Aldrich	Catalog no. K8625
CH-223191	Sigma-Aldrich	Catalog no. C8124
Collagenase, from *Clostridium histolyticum*	Sigma-Aldrich	Catalog no. C5138
Hyaluronidase from bovine testes	Sigma-Aldrich	Catalog no. H3506
PMA	Sigma-Aldrich	Catalog no. P1585
Ionomycin, Free Acid, Streptomyces conglobatus	Sigma-Aldrich	Catalog no. 407950
Dexamethasone	Sigma-Aldrich	Catalog no. D4902
Collagenase P, C. histolyt., Lyo.	Roche	Catalog no. 11249002001
DNase I recombinant, RNase-free solution	Roche	Catalog no. 4716728001
FastStart Essential DNA Green Master	Roche	Catalog no. 06924204001

(Continued)

(Continued)

Reagent	Source	Identifier
Halt(tm) Protease Inhibitor Single-Use Cocktail (100×)	Thermo Fisher Scientific	Catalog no. 00-4506-51
Monensin Solution	eBioscience	Catalog no. 00-4505-51
Propidium Iodide Staining Solution	eBioscience	Catalog no. 00-6990; RRID: 00-6990
High Potency Clophosome-Clodronate Liposomes (Anionic)	FormuMax	Catalog no. F70101C-AH
Matrigel Matrix	Corning	Catalog no. 356231
Precision Count Beads	BioLegend	Catalog no. 424902
Brilliant Stain Buffer	BD Pharmingen	Catalog no. 566349
TRIzol Reagent	Invitrogen	Catalog no. 15596018
Gibco Fetal Bovine Serum, qualified, Australia origin	Gibco	Catalog no. 10099141C
Medium 199 (1×), liquid	Gibco	Catalog no. 11150059
OPTI-MEM(R) I Reduced Serum Medium (1×)	Gibco	Catalog no. 31985070
Lymphoprep Medium 199 (1×), liquid	STEMCELL Technologies	Catalog no. 07801
Lympho Pure Medium	STEMERY	Catalog no. RC-001
NH2-PEG-N3	MeloPEG	Catalog no. 040504
HO-PCL-COOH	MeloPEG	Catalog no. 120003
Cy3	aladdin	Catalog no. C266361
Cy7	aladdin	Catalog no. C196722
Critical commercial assays		
ELISA MAX Deluxe Set Mouse IL-6	BioLegend	Catalog no. 431304
ELISA MAX Deluxe Set Mouse IL-1β	BioLegend	Catalog no. 432604
ELISA MAX Deluxe Set Mouse TNF-α	BioLegend	Catalog no. 430904
Human Tyrosine-protein kinase Mer / MERTK ELISA Kit	Genie	Catalog no. HUFI00198
EasySep Human CD8 Positive Selection Kit II	STEMCELL Technologies	Catalog no. 17853
CFSE Cell Division Tracker Kit	BioLegend	Catalog no. 423801
Zombie NIR Fixable Viability Kit	BioLegend	Catalog no. 423106
SimpleChIP Enzymatic Chromatin IP Kit (Magnetic Beads)	Cell Signaling Technology	Catalog no. 9003
Pierce BCA Protein Assay Kit	Thermo Fisher Scientific	Catalog no. 23225
pHrodo *E. coli* BioParticles conjugate for phagocytosis	Thermo Fisher Scientific	Catalog no. P35361
Revert Aid First Strand cDNA Synthesis Kit	Thermo Fisher Scientific	Catalog no. K1622
LIPOFECTAMINE 3000 Transfection Kit	Thermo Fisher Scientific	Catalog no. L3000015
FITC Annexin V Apoptosis Detection Kit I	BD Pharmingen	Catalog no. 556547
PKH26 Red Fluorescent Cell Linker Mini Kit	Sigma-Aldrich	Catalog no. MINI26-1KT
Cell Counting Kit-8 (CCK-8)	Biosharp	Catalog no. BS350A
Deposited data		
Human melanoma scRNA-seq	This paper	PRJNA996416
Data files for mouse RNA-seq	This paper	PRJNA994276
Data files for mouse ChIP-seq	This paper	PRJNA995326
Human pan-cancer CPTAC dataset	N/A	http://ualcan.path.uab.edu/
Human pan-cancer TCGA dataset	N/A	https://kmplot.com/analysis/
Human pan-cancer immune infiltration dataset	N/A	https://hiplot.com.cn/advance/ucsc-xena-shiny
Human pan-cancer immune gene dataset	N/A	http://timer.cistrome.org/
Human melanoma cohort with anti–PD-1 therapy	European Molecular Biology Laboratory–European Bioinformatics Institute	PRJEB23709

(Continued)

(Continued)

Human TCGA SKCM	N/A	www.bioinformatics.com.cn/
Experimental models: Cell lines		
B16-F10	American Type Culture Collection	Catalog no. CRL-6475
Experimental models: Organisms/strains		
C57BL/6 mice	Beijing Huafukang Bioscience Co. Inc.	N/A
$Lyz2^{cre/+}Ahr^{fl/fl}$ mice	Cyagen Biosciences Inc.	N/A

Data processing and gene expression correlation analysis

We obtained the transcriptomic profiling of a melanoma patient cohort with anti–PD-1 therapy (PRJEB23709) from the European Molecular Biology Laboratory–European Bioinformatics Institute database (www.ebi.ac.uk/ena/data/view/PRJEB23709). Gene expression correlation analyses of TCGA SKCM and PRJEB23709 were obtained by Bioinformatics (www.bioinformatics.com.cn/), an online platform for the analyses and visualization of data.

Gene expression analysis

We input MerTK in the "Gene_DE" module of TIMER2 (Tumor IMmune Estimation Resource, version 2) web (http://timer.cistrome.org/) and observed the expression difference of MerTK between tumor and adjacent normal tissues for the different tumors or specific tumor subtypes of the TCGA project.

Survival prognosis analysis

The association between gene expression and OS in pan-cancer was obtained by Kaplan-Meier Plotter (https://kmplot.com/analysis/) and melanoma patient datasets from TCGA.

Immune infiltration analysis

We analyzed the association between mRNA expression and tumor immune infiltration in pan-cancer by using the "Quick Pan-Cancer Analysis" module of UCSC Xena Shiny (https://hiplot.com.cn/advance/ucsc-xena-shiny).

RNA sequencing

Total RNA was extracted from BMDMs using TRIzol (Invitrogen) following the manufacturer's instructions. Purified mRNA was fragmented into small pieces with fragment buffer at an appropriate temperature. First-strand cDNA was generated using random hexamer-primed reverse transcription, followed by second-strand cDNA synthesis. Afterward, A-Tailing Mix and RNA Index Adapters were added by incubation to perform end repair. The cDNA fragments obtained from the previous step were amplified by PCR, and the products were purified by Ampure XP Beads, then dissolved in ethidium bromide solution. The product was validated on an Agilent Technologies 2100 bioanalyzer for quality control. The double-stranded PCR products from the previous step were denatured and circularized by the splint oligo sequence to obtain the final library. The single-strand circular DNA was formatted as the final library. The final library was amplified with phi29 to generate DNA nanoballs (DNBs), each having more than 300 copies of one molecule. The DNBs were loaded into the patterned nanoarray, and single-end 50-base reads were generated on the BGIseq500 platform (BGI, Shenzhen, China).

MDM culture and polarization

Human PBMCs from healthy donors were obtained from the Union Hospital, Tongji Medical College, HUST, Wuhan, China. Human monocytes were isolated from healthy donor PBMCs by adherence. PBMCs were suspended in serum-free RPMI 1640 media at 1×10^7 cells/ml. A total of 12.5 ml of the cell suspension was added to each 10-cm dish and incubated for 1 hour in a humidified 37°C, 5% CO_2 incubator. Medium containing nonadherent cells was discarded, and adherent monocytes were cultured in C10 media with human M-CSF (10 ng/ml; PeproTech) for 6 days to generate MDMs. At day 6, the resulting MDMs were collected and reseeded in a six-well plate in C10 medium (1×10^6 cells/2 ml per well) for 48 hours, in the presence or absence of recombinant human IL-4 (10 ng/ml; BioLegend) and human IL-13 (10 ng/ml; BioLegend) to induce MDM immunosuppressive polarization. MDMs were polarized with recombinant human IL-4 and human IL-13 for 24 hours to obtain M2-like MDM. ALKAL1 (1 μg/ml; MCE) combined with 10 μM CH223191 (Sigma-Aldrich) were added to the MDM polarization culture. Polarized MDMs were then collected and used for Western blot analysis.

BMDM culture and polarization

Mouse BMDMs were established from bone marrow cells of C57BL/6 mice. Bone marrow cells were cultured in DMEM containing 10% FBS and murine macrophage colony-stimulating factor (50 ng/ml; R&D Systems) for 5 days. At day 6, the resulting BMDMs were collected and reseeded in a 24-well plate (1×10^6 cells/ml, 500 μl per well) in DMEM containing 10% FBS for 24 hours. BMDMs were treated with IL-4 (20 ng/ml; PeproTech) to stimulate the M2 phenotype or LPS (100 ng/ml; InvivoGen) to stimulate the M1 phenotype.

Macrophage phagocytosis analysis

Thymus tissues from 4- to 6-week-old mice were collected, and single-cell suspensions were treated with 1 μM dexamethasone (Sigma-Aldrich) for 6 hours and then labeled with PKH26 (Sigma-Aldrich). Macrophages were pretreated with CH223191 (Sigma-Aldrich) at 10 μM or Kyn (Sigma-Aldrich) at 200 μM for 24 hours. The fluorescence-labeled apoptotic thymocytes were added to BMDMs in a ratio of 10:1 and cultured at 37°C for 30, 60, 90, and 180 min in RPMI 1640 medium supplemented with 10% FBS. After incubation,

unengulfed apoptotic cells were washed away, and macrophages were labeled with F4/80 and analyzed by flow cytometry (eBioscience) or confocal microscopy (Cell Signaling Technology). When BMDMs were incubated with pHrodo E.coli BioParticles conjugates (Thermo Fisher Scientific), the phagocytosis was measured using a microplate reader (Biotek Synergy H1) at an excitation wavelength of 560 nm and an emission wavelength of 585 nm.

Coculture assay for macrophages and T cells

IL-4–polarized BMDMs were mixed with splenocytes harvested from B6 wild-type mice at a 1:6 ratio and then cultured in a 24-well plate in RPMI 1640 medium (5×10^6 splenocytes/ml per well), in the presence of plate-bound anti-mouse CD3ε (3 μg/ml; eBioscience) and soluble anti-mouse CD28 (1.5 μg/ml; eBioscience) for 3 days. In some experiments, splenocytes were prelabeled with 1 μM carboxyfluorescein diacetate succinimidyl ester (BioLegend) for 10 min at 37°C following the manufacturer's protocol. At the end of the culture, cells were collected for flow cytometry analysis.

3D human tumor/TAM/T cell organoid culture

Human MDMs were generated from healthy donor PBMCs and polarized with IL-4/IL-13 in the presence or absence of CH223191 treatment. Human $CD8^+$ T cells were sorted from healthy donor human PBMC using the Human CD8 Positive Selection Kit II (STEMCELL Technologies) and stimulated with anti-CD3/CD28 (10 μg/ml; BioLegend) and IL-2 (20 ng/ml; PeproTech) for 3 days to expand human $CD8^+$ T cells in vitro. The A375 tumor cells, MDMs, and human $CD8^+$ T cells were mixed at a 2:1:2 ratio. Mixed cells were centrifuged and resuspended in C10 medium at 1×10^5 cells per microliter of medium. The cell slurry was adjusted to 5 μl per aggregate and was gently transferred onto a microporous membrane cell insert (Millicell, PICM0RG50) to form a 3D human tumor/TAM/T cell organoid. Before cell transfer, cell inserts were placed in a six-well plate immersed with 1 ml of C10 medium. Two days later, the organoids were dissociated by a P1000 pipet tip and disrupted through a 70-μm nylon strainer to generate single-cell suspensions for further analysis.

Chromatin immunoprecipitation

BMDMs were cross-linked with 1% paraformaldehyde for 10 min at room temperature. Chromatin was isolated by sequential resuspension in Farnham Lysis and radioimmunoprecipitation assay (RIPA) buffers, and subsequently fragmented with a sonifier (Branson Sonifier SFX). For immunoprecipitation, anti-mouse IgG3 (Abcam) was incubated overnight at 4°C with 10 μg of anti-AhR antibody (Thermo Fisher Scientific). The labeled beads were subsequently washed and incubated overnight with the sonicated chromatin preparation at 4°C. After immunoprecipitation, the protein-DNA cross-links were reversed by heating at 65°C, followed by proteinase K and ribonuclease A treatment. DNA was purified by extraction with phenol/chloroform/isoamyl alcohol and amplified by reverse transcription PCR (RT-PCR) with primers specific for AhR-bound regions of interest at the ALKAL1 loci, as well as an irrelevant region within each locus. Primers are listed in table S6.

ChIP-seq analysis

ChIP-seq was conducted by Igenebook (Wuhan, China). The ChIP DNA library concentrations were quantified using a Qubit 3.0 Fluorometer (Thermo Fisher Scientific), and the size of the fragments was examined with a Qsep1 Bio-Fragment Analyzer (BiOptic). Libraries were sequenced using sequencing strategy PE150 on an Illumina HiSeq X Ten System (Illumina) to obtain 20 million reads per sample. Resulting fastq files of clean reads were aligned to the human genome hg38_94 using BWA (version 0.7.15-r1140) to generate bam files. Peaks (see table S7) were called using MACS (version 2.1.1.20160309) with $P < 0.001$ and visualized with an Integrative Genomics Viewer (version 2.8.9, Broad Institute). The genes were used for further analysis. Raw data are available upon request.

Small interfering RNA transfection

Macrophages were transfected with control nontargeting small interfering RNAs (siRNAs) or specific ALKAL1 siRNAs using HiperFect transfection reagent (Qiagen) according to the manufacturer's instructions. Specifically, siRNAs and HiperFect reagents (1:2 ratio, pmol of siRNA: microliter of reagents) were dissolved in Opti-MEM medium and incubated for 5 min at room temperature. The siRNA-reagent complexes were then added to macrophages and incubated at 37°C for 6 hours. The transfection complexes were removed, and fresh media were added to the macrophages. The cells were cultured for an additional 2 days before treatment. Mouse ALKAL1 siRNAs were all purchased from Tsingke Biotechnology Co., Ltd.

In vivo macrophage adoptive transfer experiments

$MerTK^-$ macrophages ($CD45^+F4/80^+CD11b^+MerTK^-$ cells) and $MerTK^+$ macrophages ($CD45^+F4/80^+CD11b^+MerTK^+$ cells) were isolated from single-cell suspensions of mouse tumors from donor mice by FACS. In some experiments, to deplete macrophages, tumor-bearing mice were injected with control liposomes or high potency clodronate liposomes (FormuMax) according to the guidance of the manufacturer. Briefly, 20-μl high-potency clodronate liposomes were intradermally administered to tumor-bearing mice on days 6, 8, and 10. In addition, 3×10^5 $MerTK^-$ or $MerTK^+$ macrophages were adoptive transferred intravenously to recipient mice on days 12, 15, and 18 after tumor cell inoculation. In other experiments, 3×10^5 $MerTK^-$ or $MerTK^+$ macrophages were adoptive transferred intravenously to $AhR^{fl/fl}$ or $Lyz^{cre+/-}AhR^{fl/fl}$ mice on days 12, 15, and 18 after tumor cell inoculation.

Tumor growth and treatment

B16-F10 tumor–bearing mice models were established by subcutaneously implanting 1×10^5 or 3×10^5 cells in 100 μl of PBS into the lateral right flank. Treatments were given as single agents or in combinations with the following regimen for each drug. CH223191 was dissolved at 0.5% methyl cellulose and 0.5% Tween 80 in water. In some experiments, tumor-bearing mice were randomly divided into four groups, and saline, free CH223191, MMic, CH223191-MMic were administered via a tail vein injection at a dose equivalent to 0.5 mg/kg of CH223191. In some experiments, anti–PD-1 antibody (200 μg per mouse, Bio X Cell) was injected intraperitoneally every 3 days, starting from day 3 after tumor implantation. The mice that received an intraperitoneal injection of isotype antibodies (200 μg per mouse, every 3 days, Bio X Cell) were included as controls. Tumor volumes were measured every 2 days and calculated as (length × $width^2/2$). Animals were euthanized for signs of distress or when the total tumor volume reached 2000 mm^3. At the end of an experiment, solid tumors were collected, and TIIs were isolated for analysis using flow cytometry and immunofluorescence.

TII isolation and analysis

Mouse tumors were minced with scissors before incubation with collagenase IV (320 μg/ml; Sigma-Aldrich), Hyaluronidase Type V (500 μg/ml; Sigma-Aldrich), and DNase I (5 μg/ml; Sigma-Aldrich) in RPMI 1640 for 30 min at 37°C. Samples were then processed by repeated pipetting and filtered through a 70-μm cell strainer (Corning) in RPMI to generate single-cell suspensions. Immune cells were enriched through gradient centrifugation with lymphocyte pure medium (STEMERY) at 524*g* for 30 min at 25°C without braking, followed by treatment with tris-buffered ammonium chloride buffer to lyse red blood cells according to a standard protocol. The resulting TII isolates were then used for flow cytometry analysis. TIIs obtained from mouse tumors were preincubated (15 min, 4°C) with anti-CD16/32 monoclonal antibody (Fc block, BioLegend) to block nonspecific binding. Subsequently, the indicated antibodies were added, and staining was continued for 30 min on ice in the dark. For the composition of the TME determination, TAMs (pregated as $CD45^+CD11b^+F4/80^+$ cells), and $CD4^+$ (pregated as $CD45^+CD3^+CD4^+CD8^-$ cells), and $CD8^+$ (pregated as $CD45^+CD3^+CD4^-CD8^+$ cells) T cells were analyzed by spectral flow cytometry (Sony ID7000).

For intracellular cytokine production of IFN-γ, TNF-α, Granzyme B, and perforin, cells were stimulated with a cell stimulation cocktail plus protein transport inhibitors, including PMA (20 ng/ml; Sigma-Aldrich), ionomycin (1 μg/ml; Sigma-Aldrich), brefeldin A (eBioscience, 1:1000), and monensin (eBioscience, 1:1000) for 4 hours at 37°C with 5% CO_2 in RPMI medium supplemented with 10% FBS. Subsequently, cells were further permeabilized with the Cytofix/Cytoperm W/Golgi Stop Kit (BD Pharmingen) at a ratio of 1:3 for 30 min at 4°C. Antibodies were added and incubated for 1 hour at 4°C following the manufacturer's protocol.

Reverse transcription polymerase chain reaction

cDNA was prepared using 1 μg of RNA with the Revert Aid First Strand cDNA Synthesis Kit (Thermo Fisher Scientific). Real-time PCR was performed using the DNA Green Master (Roche). The primer sequences are provided in table S6. mRNA levels were normalized to β-actin (dCt = Ct gene of interest − Ct β-actin) and reported as relative mRNA expression [$ddCt = 2^{-(dCt\ sample - dCt\ control)}$] or fold change.

Western blotting

For immunoblotting analysis, whole-cell lysates were prepared in RIPA lysis buffer containing Halt Protease Inhibitor Cocktail (Thermo Fisher Scientific) for 30 min on ice. The protein concentrations were determined by BCA Protein Assay Kits (Thermo Fisher Scientific). Twenty to 60 μg of protein samples were loaded onto SDS-PAGE gels and transferred to a polyvinylidene difluoride membrane.

Immunofluorescence and confocal microscopy

BMDMs on coverslips were fixed with 4% paraformaldehyde in PBS for 30 min at room temperature, permeabilized with 0.5% Triton X-100 in PBS for 10 min at room temperature, and then blocked with PBS containing 1% bovine serum albumin and 1% goat serum for 30 min. The cells on coverslips were incubated with primary antibodies at 4°C overnight and then mounted with antifade mounting medium, placed on glass slides, and imaged using an LSM 780 laser-scanning confocal microscope (Carl Zeiss).

Immunohistochemistry, multicolor immunohistochemistry, and image analysis

Human tissue samples were fixed in formalin and embedded in paraffin. Three-micrometer sections were cut for histological analysis and stained with hematoxylin and eosin. Three-micrometer tissue sections were also used for immunostaining. The primary antibody was incubated with the tissue sections overnight at 4°C and detected with biotinylated secondary antibodies and streptavidin horseradish peroxidase (Vector). Positive signals were developed with diaminobenzidine substrate (DAKO). Quantitative analysis was performed using the image analytical software ImageJ to determine the histological changes in tumor tissue at different stages.

For multiplex immunohistochemistry, the steps used were similar. Incubation of the primary antibody followed for 30 min at 37°C. The appropriate secondary antibody was then applied for 15 min. Last, one of the tyramide signal amplification fluorophores (Akoya Biosciences) was added to the tissue slides for 8 min. Stripping of the primary and secondary antibodies was accomplished by heating the slides at 100°C in the cell conditioning solution. This sequence of steps (except for deparaffinization and antigen retrieval) was repeated for each primary antibody.

Random tumor areas of high-resolution whole-slide scanned images were first annotated in CaseViewer2.4 (3DHISTECH) and then analyzed with the Halo v3.0.311.314 (Indica Labs). HighPlex FL v3.1.0 module was used to quantify the number of total cells and coexpressed cells in each section of tumor tissue, and the positive rate (%) = number of positive cells/total cells × 100%.

Synthesis of CH223191-MMic

The Man–polyethylene glycol (PEG)–1,2-distearoyl-sn-glycero-3-phospho-ethanolamine (DSPE) was synthesized according to the method previously reported by Zhang *et al.* with minor modifications (*56*). Briefly, the efficient and simple synthesis of two families (208 mg of NH2-PEG-N3 and 218 mg of propargylated D-mannose) of mannosylated ligands having a reversed linkage was achieved through Cu(I)-catalyzed click reaction between 3-azidopropyl α-D-mannopyranoside and various alkyne-terminated substituted phenyls. The carboxylated copolymers were further conjugated with DSPE through amidation using dicyclohexylcarbodiimide as a coupling agent. Subsequently, 500 μg of CH223191 and 5 mg of Man-PEG-polycaprolactone (PCL) were dissolved in 1 ml of dimethyl sulfoxide. After the solution was mixed and stirred for 1 hour, 5 ml of ultrapure water was added to it drop by drop for 15 min. After the solution was stirred for a further 1 hour, it was transferred to a dialysis bag with a molecular weight of 2000, and dialysis was performed with 10 liters of ultrapure water for 48 hours.

Characterization of CH223191-MMic

The zeta potential of the prepared polymer micelles was measured using NanoZS Zetasizer equipment. FEI Tecnai G2 F20 TEM (Eindhoven, the Netherlands) was used to characterize the morphology of CH223191-MMic. Fluorescence spectra were obtained using an F-4600 fluorospectrometer (Hitachi).

In vivo distribution and biocompatibility

To determine the retention time of CH223191-MMic in tumors and their biodistribution in mice, fluorescence signals at tumor

sites in the tumor-bearing mice were immediately investigated using a live fluorescence imaging system (IVIS Lumina XR, Caliper, Mountain View, CA) when the mice were euthanized. The ex vivo tumors and organs (heart, liver, spleen, lung, and kidney) were then obtained by dissecting the mice and were observed using a live fluorescence imaging system to detect their fluorescence signals at an excitation wavelength of 760 nm and an emission wavelength of 790 nm.

Statistical analysis

The number of mice and statistical tests used are reported in each figure legend. All statistical analyses were performed using GraphPad Prism 8 software. Statistical significance was calculated using a *t* test (unpaired), one-way analysis of variance (ANOVA), or two-way ANOVA. Error bars represent the SEM, and *P* values <0.05 were considered statistically significant ($*P < 0.05$, $**P < 0.01$, $***P < 0.001$).

Supplementary Materials

The PDF file includes:
Figs. S1 to S10
Legends for tables S1 to S7

Other Supplementary Material for this manuscript includes the following:
Tables S1 to S7

REFERENCES AND NOTES

1. J. Y. Wang, E. B. Wang, S. M. Swetter, What is melanoma? *JAMA* **329**, 948 (2023).
2. I. Mellman, G. Coukos, G. Dranoff, Cancer immunotherapy comes of age. *Nature* **480**, 480–489 (2011).
3. Y. Zhang, Z. Zhang, The history and advances in cancer immunotherapy: Understanding the characteristics of tumor-infiltrating immune cells and their therapeutic implications. *Cell. Mol. Immunol.* **17**, 807–821 (2020).
4. R. W. Jenkins, R. Thummalapalli, J. Carter, I. Cañadas, D. A. Barbie, Molecular and genomic determinants of response to immune checkpoint inhibition in cancer. *Annu. Rev. Med.* **69**, 333–347 (2018).
5. D. R. Littman, Releasing the brakes on cancer immunotherapy. *Cell* **162**, 1186–1190 (2015).
6. S. Kalaora, A. Nagler, J. A. Wargo, Y. Samuels, Mechanisms of immune activation and regulation: Lessons from melanoma. *Nat. Rev. Cancer* **22**, 195–207 (2022).
7. J. Galon, D. Bruni, Approaches to treat immune hot, altered and cold tumours with combination immunotherapies. *Nat. Rev. Drug Discov.* **18**, 197–218 (2019).
8. L. Cassetta, T. Kitamura, Macrophage targeting: Opening new possibilities for cancer immunotherapy. *Immunology* **155**, 285–293 (2018).
9. X. Xiang, J. Wang, D. Lu, X. Xu, Targeting tumor-associated macrophages to synergize tumor immunotherapy. *Signal Transduct. Target. Ther.* **6**, 75 (2021).
10. Y. Lin, J. Xu, H. Lan, Tumor-associated macrophages in tumor metastasis: Biological roles and clinical therapeutic applications. *J. Hematol. Oncol.* **12**, 76 (2019).
11. S. K. Biswas, Metabolic reprogramming of immune cells in cancer progression. *Immunity* **43**, 435–449 (2015).
12. R. Noy, J. W. Pollard, Tumor-associated macrophages: From mechanisms to therapy. *Immunity* **41**, 49–61 (2014).
13. S. P. Arlauckas, S. B. Garren, C. S. Garris, R. H. Kohler, J. Oh, M. J. Pittet, R. Weissleder, Arg1 expression defines immunosuppressive subsets of tumor-associated macrophages. *Theranostics* **8**, 5842–5854 (2018).
14. A. Mantovani, F. Marchesi, A. Malesci, L. Laghi, P. Allavena, Tumour-associated macrophages as treatment targets in oncology. *Nat. Rev. Clin. Oncol.* **14**, 399–416 (2017).
15. C. H. June, M. Sadelain, Chimeric antigen receptor therapy. *N. Engl. J. Med.* **379**, 64–73 (2018).
16. F. Meric-Bernstam, J. Larkin, J. Tabernero, C. Bonini, Enhancing anti-tumour efficacy with immunotherapy combinations. *Lancet* **397**, 1010–1022 (2021).
17. I. Vitale, G. Manic, L. M. Coussens, G. Kroemer, L. Galluzzi, Macrophages and metabolism in the tumor microenvironment. *Cell Metab.* **30**, 36–50 (2019).
18. J. Li, I. Smalley, Z. Chen, J.-Y. Wu, M. S. Phadke, J. K. Teer, T. Nguyen, F. A. Karreth, J. M. Koomen, A. A. Sarnaik, J. S. Zager, N. I. Khushalani, A. A. Tarhini, V. K. Sondak, P. C. Rodriguez, J. L. Messina, Y. A. Chen, K. S. M. Smalley, Single-cell characterization of the cellular landscape of acral melanoma identifies novel targets for immunotherapy. *Clin. Cancer Res.* **28**, 2131–2146 (2022).
19. S. L. Park, A. Buzzai, J. Rautela, J. L. Hor, K. Hochheiser, M. Effern, N. McBain, T. Wagner, J. Edwards, R. McConville, J. S. Wilmott, R. A. Scolyer, T. Tuting, U. Palendira, D. Gyorki, S. N. Mueller, N. D. Huntington, S. Bedoui, M. Hölzel, L. K. Mackay, J. Waithman, T. Gebhardt, Tissue-resident memory $CD8^+$ T cells promote melanoma-immune equilibrium in skin. *Nature* **565**, 366–371 (2019).
20. J. Edwards, J. S. Wilmott, J. Madore, T. N. Gide, C. Quek, A. Tasker, A. Ferguson, J. Chen, R. Hewavisenti, P. Hersey, T. Gebhardt, W. Weninger, W. J. Britton, R. P. M. Saw, J. F. Thompson, A. M. Menzies, G. V. Long, R. A. Scolyer, U. Palendira, $CD103^+$ tumor-resident $CD8^+$ T cells are associated with improved survival in immunotherapy-naïve melanoma patients and expand significantly during anti-PD-1 treatment. *Clin. Cancer Res.* **24**, 3036–3045 (2018).
21. L. Cassetta, J. W. Pollard, Targeting macrophages: Therapeutic approaches in cancer. *Nat. Rev. Drug Discov.* **17**, 887–904 (2018).
22. S. Gazzaniga, A. I. Bravo, A. Guglielmotti, N. van Rooijen, F. Maschi, A. Vecchi, A. Mantovani, J. Mordoh, R. Wainstok, Targeting tumor-associated macrophages and inhibition of MCP-1 reduce angiogenesis and tumor growth in a human melanoma xenograft. *J. Invest. Dermatol.* **127**, 2031–2041 (2007).
23. E. Boada-Romero, J. Martinez, B. L. Heckmann, D. R. Green, The clearance of dead cells by efferocytosis. *Nat. Rev. Mol. Cell Biol.* **21**, 398–414 (2020).
24. J. Lin, A. Xu, J. Jin, M. Zhang, J. Lou, C. Qian, J. Zhu, Y. Wang, Z. Yang, X. Li, W. Yu, B. Liu, H. Tao, MerTK-mediated efferocytosis promotes immune tolerance and tumor progression in osteosarcoma through enhancing M2 polarization and PD-L1 expression. *Oncoimmunology* **11**, 2024941 (2022).
25. W.-S. Chung, L. E. Clarke, G. X. Wang, B. K. Stafford, A. Sher, C. Chakraborty, J. Joung, L. C. Foo, A. Thompson, C. Chen, S. J. Smith, B. A. Barres, Astrocytes mediate synapse elimination through MEGF10 and MERTK pathways. *Nature* **504**, 394–400 (2013).
26. D. Yan, J. M. Huelse, D. Kireev, Z. Tan, L. Chen, S. Goyal, X. Wang, S. V. Frye, M. Behera, F. Schneider, S. S. Ramalingam, T. Owonikoko, H. S. Earp, D. DeRyckere, D. K. Graham, MERTK activation drives osimertinib resistance in EGFR-mutant non-small cell lung cancer. *J. Clin. Invest.* **132**, e150517 (2022).
27. J. Engelmann, J. Zarrer, V. Gensch, K. Riecken, N. Berenbrok, T. V. Luu, A. Beitzen-Heineke, M. E. Vargas-Delgado, K. Pantel, C. Bokemeyer, S. Bhamidipati, I. S. Darwish, E. Masuda, T. Burstyn-Cohen, E. J. Alberto, S. Ghosh, C. Rothlin, E. Hesse, H. Taipaleenmäki, I. Ben-Batalla, S. Loges, Regulation of bone homeostasis by MERTK and TYRO3. *Nat. Commun.* **13**, 7689 (2022).
28. J. L. Schneider, J. J. Lin, A. T. Shaw, ALK-positive lung cancer: A moving target. *Nat. Cancer* **4**, 330–343 (2023).
29. S. de Munck, M. Provost, M. Kurikawa, I. Omori, J. Mukohyama, J. Felix, Y. Bloch, O. Abdel-Wahab, J. F. Bazan, A. Yoshimi, S. N. Savvides, Structural basis of cytokine-mediated activation of ALK family receptors. *Nature* **600**, 143–147 (2021).
30. A. V. Reshetnyak, P. Rossi, A. G. Myasnikov, M. Sowaileh, J. Mohanty, A. Nourse, D. J. Miller, I. Lax, J. Schlessinger, C. G. Kalodimos, Mechanism for the activation of the anaplastic lymphoma kinase receptor. *Nature* **600**, 153–157 (2021).
31. K. Hezaveh, R. S. Shinde, A. Klötgen, M. J. Halaby, S. Lamorte, M. T. Ciudad, R. Quevedo, L. Neufeld, Z. Q. Liu, R. Jin, B. T. Grünwald, E. G. Foerster, D. Chaharlangi, M. Guo, P. Makhijani, X. Zhang, T. J. Pugh, D. M. Pinto, I. L. Co, A. P. McGuigan, G. H. Jang, R. Khokha, P. S. Ohashi, G. M. O'Kane, S. Gallinger, W. W. Navarre, H. Maughan, D. J. Philpott, D. G. Brooks, T. L. McGaha, Tryptophan-derived microbial metabolites activate the aryl hydrocarbon receptor in tumor-associated macrophages to suppress anti-tumor immunity. *Immunity* **55**, 324–340.e8 (2022).
32. J. Chen, Z. Lin, L. Liu, R. Zhang, Y. Geng, M. Fan, W. Zhu, M. Lu, L. Lu, H. Jia, J. Zhang, L.-X. Qin, GOLM1 exacerbates $CD8^+$ T cell suppression in hepatocellular carcinoma by promoting exosomal PD-L1 transport into tumor-associated macrophages. *Signal Transduct. Target. Ther.* **6**, 397 (2021).
33. D. G. DeNardo, B. Ruffell, Macrophages as regulators of tumour immunity and immunotherapy. *Nat. Rev. Immunol.* **19**, 369–382 (2019).
34. R. Y. Ma, A. Black, B. Z. Qian, Macrophage diversity in cancer revisited in the era of single-cell omics. *Trends Immunol.* **43**, 546–563 (2022).
35. H. Gonzalez, C. Hagerling, Z. Werb, Roles of the immune system in cancer: From tumor initiation to metastatic progression. *Genes Dev.* **32**, 1267–1284 (2018).
36. I. A. Murray, A. D. Patterson, G. H. Perdew, Aryl hydrocarbon receptor ligands in cancer: Friend and foe. *Nat. Rev. Cancer* **14**, 801–814 (2014).
37. M. C. Takenaka, G. Gabriely, V. Rothhammer, I. D. Mascanfroni, M. A. Wheeler, C.-C. Chao, C. Gutierrez-Vazquez, J. Kenison, E. C. Tjon, A. Barroso, T. Vandeventer, K. A. de Lima, S. Rothweiler, L. Mayo, S. Ghannam, S. Zandee, L. Healy, D. Sherr, M. F. Farez, A. Prat, J. Antel, D. A. Reardon, H. Zhang, S. C. Robson, G. Getz, H. L. Weiner, F. J. Quintana, Control of tumor-associated macrophages and T cells in glioblastoma via AHR and CD39. *Nat. Neurosci.* **22**, 729–740 (2019).
38. P. Mehrotra, K. S. Ravichandran, Drugging the efferocytosis process: Concepts and opportunities. *Nat. Rev. Drug Discov.* **21**, 601–620 (2022).
39. A. C. Doran, A. Yurdagul Jr., I. Tabas, Efferocytosis in health and disease. *Nat. Rev. Immunol.* **20**, 254–267 (2020).

40. L. Zheng, J. Jia, Y. Chen, R. Liu, R. Cao, M. Duan, M. Zhang, Y. Xu, Pentoxifylline alleviates ischemic white matter injury through up-regulating Mertk-mediated myelin clearance. *J. Neuroinflammation* **19**, 128 (2022).
41. J. Zhuang, Y. Peng, C. Gu, H. Chen, Z. Lin, H. Zhou, X. Wu, J. Li, X. Yu, Y. Cao, H. Zeng, X. Fu, C. Xu, P. Huang, S. Cao, C. Wang, F. Yan, G. Chen, Wogonin accelerates hematoma clearance and improves neurological outcome via the PPAR-γ pathway after intracerebral hemorrhage. *Transl. Stroke Res.* **12**, 660–675 (2021).
42. C. Z. Han, K. S. Ravichandran, Metabolic connections during apoptotic cell engulfment. *Cell* **147**, 1442–1445 (2011).
43. R. Shinde, K. Hezaveh, M. J. Halaby, A. Kloetgen, A. Chakravarthy, T. da Silva Medina, R. Deol, K. P. Manion, Y. Baglaenko, M. Eldh, S. Lamorte, D. Wallace, S. B. Chodisetti, B. Ravishankar, H. Liu, K. Chaudhary, D. H. Munn, A. Tsirigos, M. Madaio, S. Gabrielsson, Z. Touma, J. Wither, D. D. de Carvalho, T. L. McGaha, Apoptotic cell-induced AhR activity is required for immunological tolerance and suppression of systemic lupus erythematosus in mice and humans. *Nat. Immunol.* **19**, 571–582 (2018).
44. B. Hallberg, R. H. Palmer, The role of the ALK receptor in cancer biology. *Ann. Oncol.* **27** (Suppl. 3), iii4–iii15 (2016).
45. A. V. Reshetnyak, P. B. Murray, X. Shi, E. S. Mo, J. Mohanty, F. Tome, H. Bai, M. Gunel, I. Lax, J. Schlessinger, Augmentor α and β (FAM150) are ligands of the receptor tyrosine kinases ALK and LTK: Hierarchy and specificity of ligand-receptor interactions. *Proc. Natl. Acad. Sci. U.S.A.* **112**, 15862–15867 (2015).
46. H. Zhang, L. I. Pao, A. Zhou, A. D. Brace, R. Halenbeck, A. W. Hsu, T. L. Bray, K. Hestir, E. Bosch, E. Lee, G. Wang, H. Liu, B. R. Wong, W. M. Kavanaugh, L. T. Williams, Deorphanization of the human leukocyte tyrosine kinase (LTK) receptor by a signaling screen of the extracellular proteome. *Proc. Natl. Acad. Sci. U.S.A.* **111**, 15741–15745 (2014).
47. S. Chen, B. Wang, X. Fu, Y. Liang, X. Chai, Z. Ye, R. Li, Y. He, G. Kong, J. Lian, X. Li, T. Chen, X. Zhang, X. Qiu, X. Tang, K. Zhou, B. Lin, J. Zeng, *ALKAL1* gene silencing prevents colorectal cancer progression via suppressing Sonic Hedgehog (SHH) signaling pathway. *J. Cancer* **12**, 150–162 (2021).
48. V. Davra, S. Kumar, K. Geng, D. Calianese, D. Mehta, V. Gadiyar, C. Kasikara, K. C. Lahey, Y.-J. Chang, M. Wichroski, C. Gao, M. S. de Lorenzo, S. V. Kotenko, T. Bergsbaken, P. K. Mishra, W. C. Gause, M. Quigley, T. E. Spires, R. B. Birge, Axl and Mertk receptors cooperate to promote breast cancer progression by combined oncogenic signaling and evasion of host antitumor immunity. *Cancer Res.* **81**, 698–712 (2021).
49. H. Jung, S. Y. Lee, S. Lim, H. R. Choi, Y. Choi, M. Kim, S. Kim, Y. Lee, K. H. Han, W.-S. Chung, C. H. Kim, Anti-inflammatory clearance of amyloid-β by a chimeric Gas6 fusion protein. *Nat. Med.* **28**, 1802–1812 (2022).
50. L. H. Bao, H. Sakaguchi, J. Fujimoto, T. Tamaya, Osteopontin in metastatic lesions as a prognostic marker in ovarian cancers. *J. Biomed. Sci.* **14**, 373–381 (2007).
51. J. Zhao, A. Jaffe, H. Li, O. Lindenbaum, E. Sefik, R. Jackson, X. Cheng, R. A. Flavell, Y. Kluger, Detection of differentially abundant cell subpopulations in scRNA-seq data. *Proc. Natl. Acad. Sci. U.S.A.* **118**, e2100293118 (2021).
52. A. Vandenbon, D. Diez, A clustering-independent method for finding differentially expressed genes in single-cell transcriptome data. *Nat. Commun.* **11**, 4318 (2020).
53. D. Lambrechts, E. Wauters, B. Boeckx, S. Aibar, D. Nittner, O. Burton, A. Bassez, H. Decaluwé, A. Pircher, K. Van den Eynde, B. Weynand, E. Verbeken, P. de Leyn, A. Liston, J. Vansteenkiste, P. Carmeliet, S. Aerts, B. Thienpont, Phenotype molding of stromal cells in the lung tumor microenvironment. *Nat. Med.* **24**, 1277–1289 (2018).
54. S. Cheng, Z. Li, R. Gao, B. Xing, Y. Gao, Y. Yang, S. Qin, L. Zhang, H. Ouyang, P. Du, L. Jiang, B. Zhang, Y. Yang, X. Wang, X. Ren, J.-X. Bei, X. Hu, Z. Bu, J. Ji, Z. Zhang, A pan-cancer single-cell transcriptional atlas of tumor infiltrating myeloid cells. *Cell* **184**, 792–809.e23 (2021).
55. S. Jin, C. F. Guerrero-Juarez, L. Zhang, I. Chang, R. Ramos, C.-H. Kuan, P. Myung, M. V. Plikus, Q. Nie, Inference and analysis of cell-cell communication using CellChat. *Nat. Commun.* **12**, 1088 (2021).
56. X. Zhang, X. Zang, M. Qiao, X. Zhao, H. Hu, D. Chen, Targeted delivery of dasatinib to deplete tumor-associated macrophages by mannosylated mixed micelles for tumor immunotherapy. *ACS Biomater Sci. Eng.* **6**, 5675–5684 (2020).
57. T. N. Gide, C. Quek, A. M. Menzies, A. T. Tasker, P. Shang, J. Holst, J. Madore, S. Y. Lim, R. Velickovic, M. Wongchenko, Y. Yan, S. Lo, M. S. Carlino, A. Guminski, R. P. M. Saw, A. Pang, H. M. McGuire, U. Palendira, J. F. Thompson, H. Rizos, I. P. da Silva, M. Batten, R. A. Scolyer, G. V. Long, J. S. Wilmott, Distinct immune cell populations define response to anti-PD-1 monotherapy and anti-PD-1/anti-CTLA-4 combined therapy. *Cancer Cell* **35**, 238–255.e6 (2019).

Acknowledgments: We thank R. Cui of the Skin Disease Research Institute, The 2nd Hospital and School of Medicine, Zhejiang University for critical commentary on the manuscript. We further thank Z. Tan and F. Zheng in the Immunological Laboratory of Tongji Medical College, HUST, for support and all other researchers in our laboratory for contributions. **Funding:** This work was supported by the National Natural Science Foundation of China (82130089 and 82371746), Fundamental Research Funds for the Central Universities (HUST: 2021JYCXJJ062), Key R&D Program of Hubei Province (YFXM2021000203), Major Program of Wuhan Municipal Health Commission (WX21M01), and Dawn Project in Special Project of Knowledge Innovation of Wuhan (2022020801020465). **Author contributions:** Conceptualization: J.T. Methodology: N.W., J.L., and L.L. Investigation: N.W., J.L., L.Y., L.D., and C.S. Visualization: N.W., S.S., Y.F., and E.D. Supervision: J.T., Z.T., and F.Z. Writing—original draft: N.W., and J.L. Writing—review and editing: J.T. **Competing interests:** The authors declare that they have no competing interests. **Data and materials availability:** The scRNA-seq data have been deposited in the National Center for Biotechnology Information (NCBI) databases under the following accession numbers: Sequence Read Archive (SRA): SRP450523; and BioProject: PRJNA996416. The RNA-seq data have been deposited in the SRA under accession codes SRP449629 and PRJNA994276. The ChIP-seq data have been deposited in the SRA under accession codes SRP449715 and PRJNA995326. All data needed to evaluate the conclusions in the paper are present in the paper and/or the Supplementary Materials.

Submitted 23 February 2024
Accepted 30 August 2024
Published 4 October 2024
10.1126/sciadv.ado8366